

LINKING THE SPIN EVOLUTION OF MASSIVE BLACK HOLES TO GALAXY KINEMATICS

A. SESANA¹, E. BARAUSSE^{2,3}, M. DOTTI^{4,5}, AND E. M. ROSSI⁶

¹ Max Planck Institute for Gravitational Physics, Albert Einstein Institute, Am Mühlenberg 1, D-14476, Golm, Germany; alberto.sesana@aei.mpg.de

² CNRS, UMR 7095, Institut d'Astrophysique de Paris, 98bis Bd Arago, F-75014 Paris, France; barausse@iap.fr

³ Sorbonne Universités, UPMC Univ Paris 06, UMR 7095, 98bis Bd Arago, F-75014 Paris, France

⁴ Dipartimento di Fisica G. Occhialini, Università degli Studi di Milano Bicocca, Piazza della Scienza 3, I-20126 Milano, Italy; massimo.dotti@mib.infn.it

⁵ INFN, Sezione di Milano-Bicocca, Piazza della Scienza 3, I-20126 Milano, Italy

⁶ Leiden Observatory, Leiden University, P.O. Box 9513, 2300 RA Leiden, The Netherlands; emr@strw.leidenuniv.nl

Received 2014 February 28; accepted 2014 August 12; published 2014 September 29

ABSTRACT

We present the results of a semianalytical model that evolves the masses and spins of massive black holes together with the properties of their host galaxies across the cosmic history. As a consistency check, our model broadly reproduces a number of observations, e.g., the cosmic star formation history; the black hole mass, luminosity, and galaxy mass functions at low redshift; the black hole–bulge mass relation; and the morphological distribution at low redshift. For the first time in a semianalytical investigation, we relax the simplifying assumptions of perfect coherency or perfect isotropy of the gas fueling the black holes. The dynamics of gas is instead linked to the morphological properties of the host galaxies, resulting in different spin distributions for black holes hosted in different galaxy types. We compare our results with the observed sample of spin measurements obtained through broad $K\alpha$ iron line fitting. The observational data disfavor both accretion along a fixed direction and isotropic fueling. Conversely, when the properties of the accretion flow are anchored to the kinematics of the host galaxy, we obtain a good match between theoretical expectations and observations. A mixture of coherent accretion and phases of activity in which the gas dynamics is similar to that of the stars in bulges (i.e., with a significant velocity dispersion superimposed to a net rotation) best describes the data, adding further evidence in support of the coevolution of massive black holes and their hosts.

Key words: accretion, accretion disks – black hole physics – galaxies: active – galaxies: evolution – galaxies: kinematics and dynamics – quasars: supermassive black holes

Online-only material: color figures

1. INTRODUCTION

Observational evidence for the existence of massive black holes (MBHs) in the center of galaxies is circumstantial but convincing. Stellar orbits near the Galactic center point at the presence of a dark and massive object, which is too heavy and compact to be a cluster of low-luminosity bodies (Maoz 1998) or a fermion star (Schödel et al. 2002). Also, near-infrared observations of this object show that it is likely to have an event horizon because if it did not, it would emit thermal radiation and be more luminous than observed (Broderick et al. 2009; Broderick & Narayan 2006). This disfavors exotic horizonless alternatives to general relativity's black holes such as, e.g., boson stars and gravastars. Similarly, MBHs are expected to be present in the center of most galaxies (and not just ours), as their presence is required to explain quasars (QSOs), active galactic nuclei (AGNs; Soltan 1982), and the cosmic downsizing (Scannapieco et al. 2005; Croton et al. 2006; Bower et al. 2006). Indeed, observations of nuclear stellar and gas dynamics, reverberation mapping, spectroscopic single-epoch measurements, and spectral energy distribution (SED) fitting (see, e.g., Ghez et al. 2008; Gillessen et al. 2009; Kormendy & Richstone 1995; Miyoshi et al. 1995; Hicks & Malkan 2008; Blandford & McKee 1982; Kaspi et al. 2005; Calderone et al. 2013; Castignani et al. 2013 and references therein for a discussion of the different methods) corroborate this expectation and allow the mass of MBHs to be estimated. Furthermore, these MBH mass measurements have in turn resulted in the discovery of the MBH–galaxy relations (e.g., Gebhardt et al. 2000; Ferrarese & Merritt 2000; Marconi & Hunt 2003; Häring & Rix 2004; Gültekin et al. 2009), hinting at a symbiotic evolution of the central compact object and its host galaxy.

MBHs are also expected to possess a spin-angular momentum. The combination of mass and spin completely characterizes these objects if they are described by the black hole solutions of general relativity (Kerr 1963).⁷ If instead the gravity theory describing our universe is not exactly given by general relativity, other charges may be needed to describe MBHs, but the spin will still be one of them (see Barausse & Sotiriou 2013; Yagi et al. 2012; Pani et al. 2011; Pani & Cardoso 2009, for a few examples of black holes in alternative gravity theories). Indeed, future space-based gravitational wave interferometers such as ESA's L3 experiment *eLISA* (The *eLISA* Consortium et al. 2013) will measure MBH masses and spins with fantastic accuracy ($\sim 0.1\%$ and $\sim 1\%$, respectively) and also put general relativity to the test by, e.g., measuring possible additional black hole charges. More importantly from an astrophysical point of view, measurements of MBH spins could unveil still unknown links between the MBHs and their galactic hosts. As an example, knowledge of the spins could constrain the properties of the gas accreting onto the MBHs, e.g., whether it spirals toward it on a preferential plane, on completely isotropic directions, or with other more complex dynamics (Dotti et al. 2013, hereinafter D13).

Until *eLISA* or a similar space-based gravitational wave interferometer is launched, however, measuring the spins of MBHs is considerably more difficult than measuring their

⁷ Black holes in general relativity can also have an electric charge (Newman et al. 1965), but that is expected to be quickly canceled by the charges in the plasma surrounding astrophysical black holes, as well as by quantum effects such as Schwinger pair production (Gibbons 1975; Hanni 1982) or vacuum breakdown mechanisms triggering cascades of electron–positron pairs (Goldreich & Julian 1969; Ruderman & Sutherland 1975; Blandford & Znajek 1977).

masses. This is because the spin affects the dynamics of stars and gas surrounding the MBH only at distances that are orders of magnitude smaller than the MBH influence radius (e.g., Bardeen & Petterson 1975). Currently, the most accurate way of measuring the spins of MBHs is through the spectra of relativistically broadened $K\alpha$ iron lines (see Reynolds 2014; Brenneman 2013 for recent reviews on the topic). Indeed, using current X-ray spectrographs (in particular, *XMM* and *Suzaku*), a significant sample of MBHs with spin estimates is being built up. Also, more stringent constraints on the spin estimates are becoming available from hard X-ray data from *NuSTAR* (Risaliti et al. 2013; Marinucci et al. 2014a, 2014b). Finally, spin measurements with $K\alpha$ iron lines are one of the main scientific drivers of ESA’s upcoming L2 mission, *ATHENA+* (Nandra et al. 2013).

This situation calls for a theoretical framework capable of interpreting available data for MBH spins and making testable predictions for future measurements. However, detailed modeling of the MBH spin evolution is still missing. Since the spin is a vector, any theoretical model should take the evolution of its direction into account, because that also affects the evolution of the magnitude. This is particularly clear when one considers MBH mergers, which are expected in the late stages of galaxy mergers (e.g., Begelman et al. 1980). The final spin, mass, and kick velocity of the resulting MBH remnant critically depend on the orientations of the spins of the progenitors (Rezzolla et al. 2008; Barausse & Rezzolla 2009; Buonanno et al. 2008; Barausse et al. 2012; Lousto & Zlochower 2009; van Meter et al. 2010).

The main driver of the MBH evolution, however, is not expected to be given by mergers but rather by radiative efficient gas accretion (Soltan 1982; Merloni et al. 2004; Shankar et al. 2004, 2013; Wang et al. 2009; Li et al. 2012). In this case, the spin magnitude evolution depends on whether the gas in the very central regions of the accretion disk is corotating or counterrotating relative to the MBH spin. This, in turn, depends on the larger-scale geometry of the fueling process (i.e., if the gas keeps falling toward the MBH on some preferential plane), as well as on the possible realignment of the MBH–disk system due to the Bardeen–Petterson effect (Bardeen & Petterson 1975). The latter is the interplay between the frame dragging from the rotating spacetime geometry and the viscous stresses in the disk. The details of the effect of the spacetime’s geometry on the properties of accretion disks are still not completely understood (see, e.g., Sorathia et al. 2013a, 2013b and references therein). All the studies that follow the coupled evolution of the magnitude and direction of the MBH spin have been performed under some simplifying hypotheses: i.e., assuming that the disk has isotropic viscosity (see the discussion in Sorathia et al. 2013a, 2013b), using order of magnitude estimates for the effect of the alignment (e.g., King & Pringle 2006), or under the small-deformation approximation for the warped disk (e.g., Perego et al. 2009).

These simplifying hypotheses allowed for simple recipes for the spin evolution that have been used in semianalytical models of structure formation and evolution (see, e.g., Volonteri et al. 2005, 2007, 2013; Berti & Volonteri 2008; Lagos et al. 2009; Fanidakis et al. 2011, 2012; Barausse 2012). However, most of these studies (Volonteri et al. 2005; Berti & Volonteri 2008; Lagos et al. 2009; Fanidakis et al. 2011, 2012) assume that the MBH fueling is either always coherent (i.e., accretion always occurs exactly on the equatorial plane) or statistically isotropic (i.e., the MBH accretes small gas clouds with randomly oriented

angular momenta). These assumptions were partly relaxed in Barausse (2012) and Volonteri et al. (2007, 2013), who noted that the Bardeen–Petterson effect is likely to align the MBH spin with the angular momentum of the accreting gas in gas-rich nuclear environments, thus making the accretion flow effectively coherent in such situations, as opposed to isotropic accretion, which is more likely in gas-poor nuclear environments. Even with this improvement, however, the possible parameter space of the accretion flow is still limited to two points (coherent accretion in gas-rich environments versus isotropic accretion in gas-poor environments).

Recently, D13 demonstrated that the spin evolution can be significantly different if a more realistic description of the accretion flow is adopted, namely, one that allows regimes intermediate between a perfectly coherent and a perfectly isotropic flow. Dubois et al. (2014a) studied the evolution of the spins of a population of MBHs, taking into consideration the dynamical properties of the fueling gas. They extracted the direction of the angular momentum of the accreting matter on the smallest scales resolved by hydrodynamical simulations (down to ≈ 10 pc in their highest-resolution run). In a similar spirit, in this paper we couple the semianalytical model of Barausse (2012, hereinafter B12) to the spin evolution model of D13. In particular, we link the degree of coherency/isotropy of the accretion flow to the dynamical parameters of the gas and stars observed in galactic nuclei. We stress that also in our case, most of the observations that we use have a spatial resolution $\gtrsim 100$ pc, significantly larger than typical accretion disk scales, and that the dynamical properties of the gas could change at smaller unresolved scales (e.g., Hopkins et al. 2012; Maio et al. 2013; Dubois et al. 2014b). In this sense, therefore, a comparison of the predictions of our model for the MBH spin evolution with actual spin measurements provides a way of testing the dynamics and coherency of the nuclear gas at yet unresolved scales. We attempt such a test with the MBH spin measurements from $K\alpha$ iron lines available to date. We note, however, that our model provides a flexible framework to also interpret future, more accurate measurements from experiments such as *eLISA* and *ATHENA+*.

The paper is organized as follows. In Section 2 we present the details of our model for the evolution of MBHs in their galactic hosts. Improving on B12, we adopt a different star formation law (see Section 2.1 and Appendix A) and, more importantly, we update the prescription for the evolution of the MBH spins under accretion, following D13 (see Section 2.2). The degree of coherence of the accretion flow is then linked to the kinematic properties of the host galaxy in Section 3. We consider, in particular, three models: one where the degree of coherence is related to the gas kinematics, one that links it to the stellar kinematics, and a hybrid model where information from both the gas and stellar kinematics is used. In Section 4, we calibrate the free parameters of our semianalytical galaxy formation model against observations. We present our predictions for the evolution of MBH spins in Section 5, and in Section 6 we compare them to measurements from $K\alpha$ iron line profiles. In Section 7 we draw our conclusions.

2. MODEL

Our model is based on B12, who studied the cosmic evolution of MBH masses and spins using a state-of-the-art semianalytical galaxy formation model. More specifically, B12 describes the dark-matter evolution by merger trees produced with the

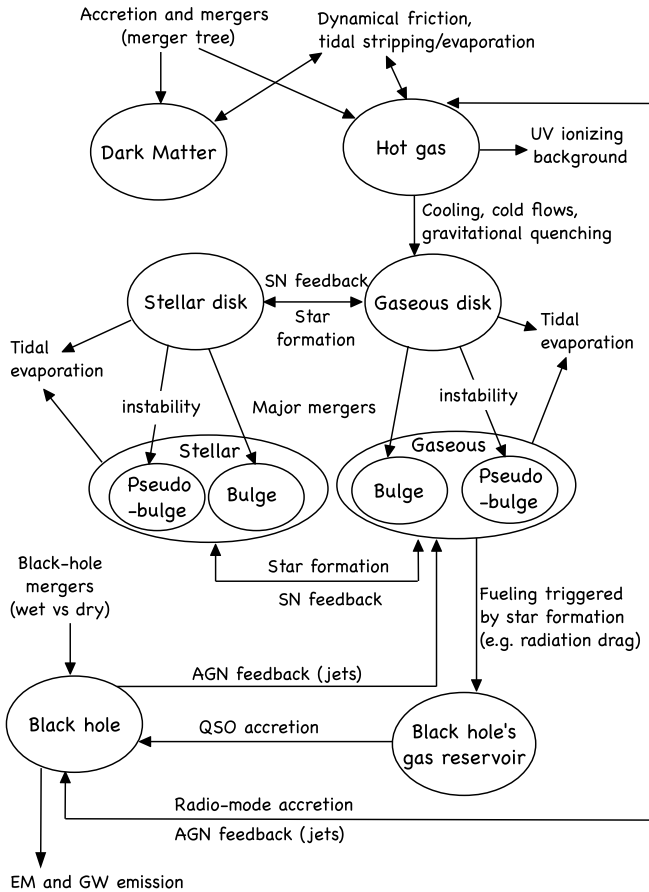


Figure 1. Schematic representation of our semianalytical model, based on that of B12. Note that B12 did not use the distinction between “bulges” forming from major galactic mergers and “pseudobulges” forming from bar instabilities of disk galaxies (although both formation channels were present). In this paper, instead, we assume that bulges and pseudobulges have different star formation laws (see Section 2.1) and, in some realizations of our model, different accretion properties onto the central MBH (see Section 3). The other major change from the model of B12 is indeed the prescription for the spin evolution of MBHs under accretion and mergers, which is schematically represented in Figure 2 and described in detail in Section 2.2.

extended Press–Schechter formalism and suitably modified to reproduce the results of N-body dark-matter simulations (Cole et al. 2008). The baryonic content of galaxies is evolved along the branches of the merger tree and includes several components: a hot-gas phase, a cold-gas disk, a stellar disk, a cold-gas bulge, a stellar bulge, a MBH, and a reservoir of cold gas fueling accretion onto the MBH. Gravitational interactions among the various components are accounted for (although in simplified ways), allowing the computation of the density and velocity profiles of the various components inside each galaxy. Also modeled are a variety of nongravitational interactions, which are summarized schematically in Figure 1.

For more details, we refer the reader to B12. Here, we focus instead on our improvements to that model: the star formation law (Section 2.1) and the description of the cosmic MBH spin evolution (Section 2.2).

2.1. Star Formation Model

The star formation model adopted here differs from and improves on the one used in B12. In this section, we describe the general framework and main equations and confine a more detailed presentation to Appendix A.

The first new ingredient is that the star formation is now an explicit function of metallicity, which allows for better modeling of the buildup of stars in different galaxies at various redshifts and environments (see the star formation history of Figure 9, to be compared with Figure 8 of B12). The second is a different prescription for *classical bulges* and *pseudobulges*. The former are the result of major galactic mergers, which cause bursts of star formation (Daddi et al. 2010; Genzel et al. 2010), while the latter result from bar instabilities in galactic disks and undergo a slower, disk-like star formation (see, e.g., Kormendy 2013). In B12, both bar instabilities and major mergers were modeled, but star formation in the bulge component was the same irrespective of the bulge’s formation mechanism. In practice, our new prescription is based on the work by Krumholz et al. (2009), extended to include the low metallicity (less than 1% solar; Krumholz & Gnedin 2011; Krumholz 2012; Forbes et al. 2014; Kuhlen et al. 2013) and starburst regimes (Daddi et al. 2010; Genzel et al. 2010).

In galactic disks, the star formation density rate is expressed in terms of the fraction f_c of the background gas surface density (Σ_g) that is converted into stars on a timescale t_{SF} ,

$$\dot{\Sigma}_* = \frac{f_c \Sigma_g}{t_{SF}}. \quad (1)$$

The metallicity dependence enters explicitly in the fraction f_c (see Equation (A4) in Appendix A): down to 2% solar, the lower the metallicity, the smaller the amount of gas available for star-forming. The timescale t_{SF} (see Equation (A2) in Appendix A) depends on the properties of giant molecular clouds (GMCs), which vary with the gas richness of the environment. This timescale is generally longer than the local free fall timescale. The same star formation law applies to pseudobulges, but it is calculated per unit volume,

$$\dot{\rho}_* = \frac{f_c \rho_g}{t_{SF}}. \quad (2)$$

Finally, in classical bulges, we describe the burst of star formation as the sudden consumption of gas in a local dynamical timescale,

$$\dot{\rho}_* = \frac{\rho_g}{t_{ff}}, \quad (3)$$

where $t_{ff} = \sqrt{3\pi/(32G\rho_g)}$.

The total star formation rates are then performed by integrating Equations (1)–(3) over the whole disk/pseudobulge/bulge.

2.2. Spin Evolution

Two main processes drive the cosmic evolution of MBH spins: *gas accretion* from the interstellar medium (ISM) or the intergalactic medium (IGM) and *mergers* between MBHs.

2.2.1. Gas Accretion

Accretion is believed to be the main driver of the MBH spin evolution (Berti & Volonteri 2008; B12), with the possible exception of the most MBHs in massive, gas-poor, low-redshift ellipticals (e.g., Fanidakis et al. 2011). Because of the spin’s vectorial nature, its evolution depends on the angular momentum magnitude and direction of the accreting gas. In our implementation, based on D13, the circumnuclear gas reservoir surrounding the MBH is accreted in a sequence of clouds, with a nontrivial angular momentum distribution. Unlike in D13, however, this

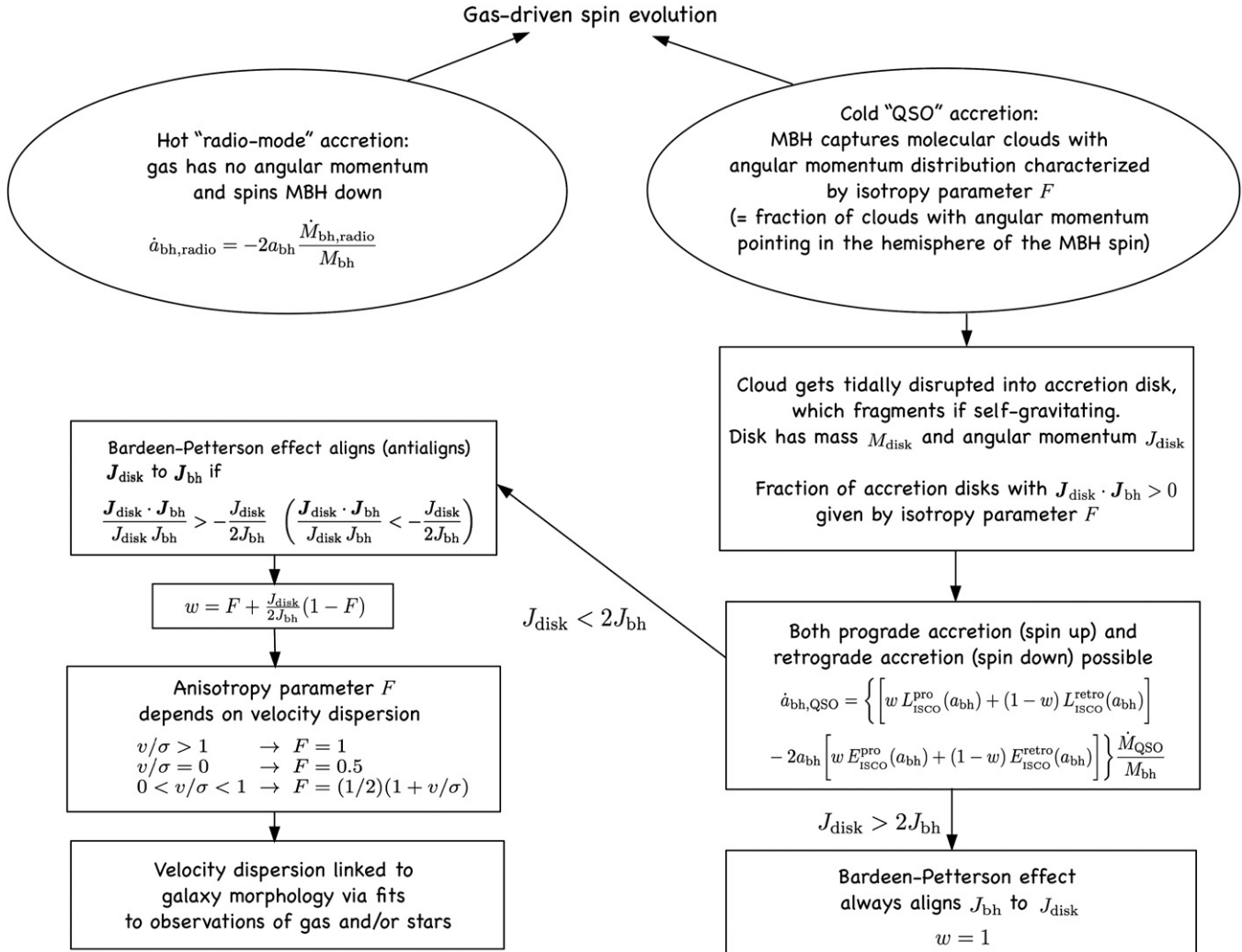


Figure 2. Scheme of the possible accretion-driven MBH spin evolution channels.

distribution is not arbitrary but is linked to the galactic properties at larger scales and therefore intimately connected to the galaxy morphology (see Section 3).

Following B12, we distinguish two main astrophysical modes of gas accretion, which prompt different spin evolution channels as illustrated in Figure 2.

1. A hot “radio” mode. In this regime, the MBH accretes IGM gas that cools on a timescale longer than its free fall time. The gas is approximately spherically symmetric, so no net angular momentum is acquired by the MBH, and the spin parameter a_{bh} changes (to first approximation) only because of the increase of the MBH mass:

$$\dot{a}_{\text{bh,radio}} = -2a_{\text{bh}} \frac{\dot{M}_{\text{bh,radio}}}{M_{\text{bh}}}, \quad (4)$$

where $\dot{M}_{\text{bh,radio}}$ is the Bondi accretion rate of the hot IGM component (see Equation (44) in B12). This mode has a negligible direct impact on the mass and spin evolution of MBHs because it is typically characterized by very low accretion rates but plays a major role in activating jets capable of exerting an “AGN feedback” on the growth of large cosmic structures (see B12 for more details on the implementation of AGN feedback).

2. A cold “QSO” mode. It is associated with the star formation in the bulge, which drives cold ISM gas into a low-angular-momentum reservoir of mass M_{res} , available for accretion onto the MBH. In practice, we assume that the influx of gas into the reservoir is proportional to the bulge star formation rate (see B12; Granato et al. 2004; Haiman et al. 2004; Lapi et al. 2014). As a result, in our current framework for the star formation (Section 2.1), major mergers tend to produce larger reservoirs and MBH accretion rates than disk instabilities. Once the cold gas has settled in the reservoir, we follow Granato et al. (2004) and assume that it accretes onto the MBH with instantaneous rate,

$$\dot{M}_{\text{QSO}} = \min(\dot{M}_{\text{visc}}, A_{\text{Edd}} \dot{M}_{\text{Edd}}). \quad (5)$$

The viscously driven accretion rate reads $\dot{M}_{\text{visc}} = k_{\text{accr}} \sigma^3 M_{\text{res}} / (GM_{\text{bh}})$, where⁸ $k_{\text{accr}} = 10^{-3}$, $\sigma = 0.65 V_{\text{vir}}$ and V_{vir} is the halo’s virial velocity (Granato et al. 2004; G. L. Granato, 2009 private communication). The Eddington rate $\dot{M}_{\text{Edd}} = L_{\text{Edd}} / [\eta (a_{\text{bh}} c^2)]$ is derived from the Eddington luminosity L_{Edd} , assuming a radiation efficiency η . As shown below (see Equation (12)), η can be computed as a function of the MBH

⁸ Note that k_{accr} is related to the critical Reynolds number $\mathcal{R}_{\text{crit}}$ for the onset of turbulence by $k_{\text{accr}} = 1/\mathcal{R}_{\text{crit}}$.

spin and the fraction of prograde vs. retrograde accretion events. The free parameter $A_{\text{Edd}} \geq 1$ sets the amount of super-Eddington accretion allowed in our model. This prescription for \dot{M}_{QSO} replaces the simpler recipe of B12, which assumed $\dot{M}_{\text{QSO}} = M_{\text{res}}/t_{\text{accr}}$, with t_{accr} a free parameter on the order of 5×10^8 yr.

The main difference with respect to B12 consists in *how* the gas in the reservoir is accreted. In B12, depending on the ratio $M_{\text{res}}/M_{\text{bh}}$, M_{res} is either accreted coherently or as a collection of small randomly oriented clouds with vanishing total angular momentum. Here, we employ a model that allows for a broader range of configurations for the accreting flow, as we proceed to explain. This model is based on results by Perego et al. (2009) and D13, to which we refer for more details.

Accretion is described as a series of transient accretion disks, each one formed following the tidal disruption of a cloud. The mass M_{disk} of each individual disk is the minimum between the typical mass of a molecular cloud— $M_{\text{cloud}} = 3 \times 10^4 M_{\odot}$ is our fiducial value—and the mass M_{sg} of a disk truncated at the self-gravity radius, where the Toomre parameter Q reaches a value of 1. This is because outside this radius, the accretion disk that forms from the infalling cloud will fragment under its self-gravity and be consumed by star formation. The explicit expression for M_{sg} is given by (D13)

$$M_{\text{sg}} \approx 2 \times 10^4 \alpha_{0.1}^{-1/45} \left(\frac{f_{\text{Edd}}}{\eta_{0.1}} \right)^{4/45} \left(\frac{M_{\text{bh}}}{10^6 M_{\odot}} \right)^{34/45} M_{\odot}, \quad (6)$$

where f_{Edd} is the Eddington ratio, $\eta_{0.1}$ is the disk radiative efficiency normalized to 0.1, and $\alpha_{0.1}$ is the disk viscosity parameter in units of 0.1. Throughout this paper we assume $\alpha_{0.1} = 1$. Each accreting lump gets tidally disrupted and settles in a standard thin accretion disk with an associated angular momentum J_{disk} obtained from its mass, $M_{\text{disk}} = \min(M_{\text{cloud}}, M_{\text{sg}})$:

$$J_{\text{disk}} = \frac{8}{21} \frac{\dot{M}_{\text{bh,QSO}} \sqrt{GM_{\text{bh}}}}{A_{\text{v}}} R_{\text{disk}}^{7/4} \quad (7)$$

$$A_{\text{v}} = 9.14 \times 10^6 \alpha_{0.1}^{4/5} \left(\frac{M_{\text{bh}}}{10^6 M_{\odot}} \right)^{1/20} \times \left(\frac{f_{\text{Edd}}}{\eta_{0.1}} \right)^{3/10} \text{cm}^{5/4} \text{s}^{-1} \quad (8)$$

(see D13). The extension of the disk R_{disk} depends on its mass. If $M_{\text{sg}} < M_{\text{cloud}}$, it is given by (D13)

$$R_{\text{disk}} \approx 10^5 R_{\text{g}} \alpha_{0.1}^{28/45} \left(\frac{M_{\text{bh}}}{10^6 M_{\odot}} \right)^{-52/45} \left(\frac{f_{\text{Edd}}}{\eta_{0.1}} \right)^{-22/45}, \quad (9)$$

where $R_{\text{g}} = 2GM_{\text{bh}}/c^2$ is the Schwarzschild radius. If instead $M_{\text{sg}} > M_{\text{cloud}}$, one has (D13)

$$R_{\text{disk}} \approx 4 \times 10^4 R_{\text{g}} \left(\frac{M_{\text{disk}}}{10^4 M_{\odot}} \right)^{4/5} \alpha_{0.1}^{16/25} \times \left(\frac{M_{\text{bh}}}{10^6 M_{\odot}} \right)^{-44/25} \left(\frac{f_{\text{Edd}}}{\eta_{0.1}} \right)^{-14/25}. \quad (10)$$

According to the initial direction of the lump’s angular momentum, the Bardeen–Petterson effect will either align or antialign the disk and the MBH spin directions (see Equation (13)),

resulting in prograde or retrograde accretion, respectively. As the total mass in the reservoir is consumed by several lumps accreting onto the MBH, the time-averaged spin evolution is determined by the fraction w ($1 - w$) of lumps that accrete on prograde (retrograde) orbits:

$$\begin{aligned} \dot{a}_{\text{bh,QSO}} = & \left[\left[w L_{\text{ISCO}}^{\text{pro}}(a_{\text{bh}}) + (1 - w) L_{\text{ISCO}}^{\text{retro}}(a_{\text{bh}}) \right] \right. \\ & \left. - 2a_{\text{bh}} \left[w E_{\text{ISCO}}^{\text{pro}}(a_{\text{bh}}) + (1 - w) E_{\text{ISCO}}^{\text{retro}}(a_{\text{bh}}) \right] \right] \frac{\dot{M}_{\text{QSO}}}{M_{\text{bh}}}, \end{aligned} \quad (11)$$

where $L_{\text{ISCO}}^{\text{pro}}(a_{\text{bh}})$ and $E_{\text{ISCO}}^{\text{pro}}(a_{\text{bh}})$ are the specific angular momentum and specific energy at the prograde innermost stable circular orbit (ISCO), respectively, while $L_{\text{ISCO}}^{\text{retro}}(a_{\text{bh}})$ and $E_{\text{ISCO}}^{\text{retro}}(a_{\text{bh}})$ are the same quantities for the retrograde ISCO. Likewise, the accretion efficiency is calculated by weighing the prograde and retrograde thin-disk efficiencies $\eta_{\text{pro}}(a_{\text{bh}})$ and $\eta_{\text{retro}}(a_{\text{bh}})$:

$$\eta(a_{\text{bh}}) = w \eta_{\text{pro}}(a_{\text{bh}}) + (1 - w) \eta_{\text{retro}}(a_{\text{bh}}). \quad (12)$$

The fraction w of prograde accretion disks is determined by the Bardeen–Petterson effect (Bardeen & Petterson 1975; King et al. 2005; King & Pringle 2006; Perego et al. 2009; D13) and is given by

$$w = \begin{cases} 1 & \text{if } J_{\text{disk}} > 2J_{\text{bh}}, \\ F + \frac{J_{\text{disk}}}{2J_{\text{bh}}}(1 - F) & \text{if } J_{\text{disk}} < 2J_{\text{bh}}. \end{cases} \quad (13)$$

Here, the “isotropy parameter” F measures the fraction of accretion events with angular momentum initially pointing in the hemisphere of the MBH spin (i.e., with angular momentum initially tilted by an angle $\theta_{\text{out}} < \pi/2$ relative to the MBH spin).⁹ When $J_{\text{disk}} > 2J_{\text{bh}}$, the MBH spin aligns with the angular momentum of the outer regions of the accretion disk that forms when the lump of matter falls into the MBH, and the alignment happens on a timescale smaller than the accretion timescale (Perego et al. 2009; D13). Most of the accreted gas then has angular momentum aligned with the MBH spin, hence $w = 1$, and the MBH spins up. In this limiting case, Equation (11) tends to Equation (38) of B12. If instead $J_{\text{disk}} < 2J_{\text{bh}}$, King et al. (2005) and King & Pringle (2006) showed that on a similarly short timescale, the inner accretion flow’s angular momentum *antialigns* with the MBH spin if the angle between the outer disk angular momentum and the MBH spin satisfies $\theta_{\text{out}} > \pi/2$ and $\cos \theta_{\text{out}} < -J_{\text{disk}}/(2J_{\text{bh}})$. Assuming the fraction $1 - F$ of accretion events with $\theta_{\text{out}} > \pi/2$ is distributed isotropically, one then obtains the second expression for w in Equation (13).

Note that in the limit of $J_{\text{disk}}/2J_{\text{bh}} \ll 1$ (always valid for very massive MBHs, $M_{\text{bh}} \gtrsim 10^9 M_{\odot}$), our model becomes very simple, as it predicts that the MBHs will move toward an equilibrium spin parameter a_{eq} function of F , obtained by setting $\dot{a}_{\text{bh,QSO}} = 0$ in Equation (11) after substituting w with F as given by Equation (13). The value of a_{eq} as a function of F is shown in Figure 3.

At this point, however, we should stress that Equations (11) and (13) (1) only provide an “averaged” version of the stochastic scenario proposed by D13: i.e., our prescription does not follow each individual accreting cloud but only approximates the model of D13 over many such clouds and (2) do not take into account

⁹ Note that D13 assumes the opposite definition for F , which is there defined as the fraction of accretion events with angular momentum initially tilted by an angle $\theta_{\text{out}} > \pi/2$, relative to the MBH spin.

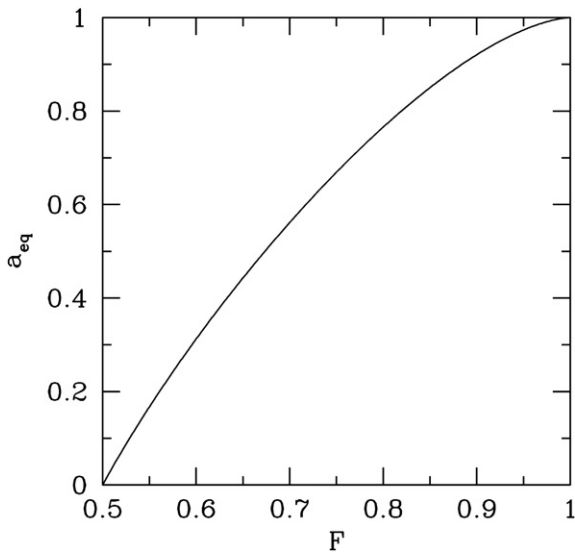


Figure 3. Equilibrium spin parameter as a function of the “isotropy parameter” F . Here we assume that each single-accretion episode has a very small angular momentum compared to the MBH, so that both alignment and antialignment can occur (see the text for details), respectively.

the detailed evolution of the accretion disk during the (short) alignment process, respectively¹⁰ A more accurate treatment of the spin evolution addressing these two shortfalls is beyond the scope of the paper, but we expect the impact of these simplifications on the spin evolution to be small. Regarding (1), the mass M_{res} of the reservoir available for accretion is typically much larger than M_{disk} ; thus accretion takes place in several “lumps,” and the stochastic character of the model of D13 averages out. An exception is in the “tails” of the accretion process, when M_{res} is small before and after a QSO event. In those tails, however, accretion rates and spin changes are small due to the scarcity of gas. We have indeed tested that replacing $M_{\text{cloud}} \rightarrow \min(M_{\text{res}}, M_{\text{cloud}})$, which corresponds to changing our model prescription in the tails of the accretion process, does not alter our results significantly. As for (2), neglecting the short alignment process is typically justified, as the alignment takes place on timescales shorter than accretion. Nevertheless, even a small amount of retrograde accretion during the alignment can potentially lower the spin significantly near the $a_{\text{bh}} = 1$ limit; more details on this point are given in Appendix C.

2.2.2. MBH Mergers

Our prescription for MBH mergers closely follows that of B12, to which we refer for more details. In summary, we use the phenomenological formulae of Barausse & Rezzolla (2009) and van Meter et al. (2010) to predict the final spin and recoil velocity of the MBH resulting from the merger and check whether the recoil ejects the MBH from the galaxy. As for the mass of the MBH produced by the merger, we update the prescription of B12 by adopting the phenomenological formula of Barausse et al. (2012). We stress that these formulae produce results in accurate agreement with fully general relativistic simulations. The only other change from the implementation of B12 regards the criterion adopted to discriminate “wet” (i.e., gas-rich) mergers from “dry” (i.e., gas-poor) mergers. This distinction is important because in wet mergers the spins of the two MBHs are expected

to align to each other—we follow here Dotti et al. (2010) and assume that the MBH spins are almost aligned, to within $\sim 10^\circ$, by the circumbinary disk via the Bardeen–Petterson effect—whereas in dry mergers such alignment does not take place, and the spins are isotropically distributed. Improving on B12, who compared M_{res} to the mass of the MBH binary to distinguish the two regimes, here we assume that a merger happens with almost aligned spins if $J_{\text{res}} > 2(S_1 + S_2)$ (where J_{res} is the angular momentum of the cold-gas reservoir, and $S_{1,2}$ are the spins of the two MBHs), while otherwise we assume that the spins are randomly oriented. This prescription is preferable to that of B12 because the Bardeen–Petterson effect is sensitive to the angular momenta of the circumbinary disk and the MBHs, rather than to their masses.

3. LINK BETWEEN ACCRETION FLOWS AND HOST DYNAMICS

In the previous section, we described how to physically relate the degree of anisotropy of the accretion flow to the MBH spin changes. The details of this relation may still need to be understood, but there is a general consensus in the community on the overall physical picture (Bardeen & Petterson 1975; King et al. 2005; King & Pringle 2006; Perego et al. 2009; D13). The outstanding question instead is what are the *actual* conditions of the flow at subparsec scales and what determines these conditions. This problem is considerably harder to solve because (1) there is hardly any direct observational evidence at those scales and (2) those scales are extremely challenging to explore theoretically with galaxy formation simulations due to lack of resolution and the unknown role of dissipative/nonlinear processes.

In an attempt to contribute some insight into the problem, we link the dynamical properties of the host galaxies, *which can be easily observed*, to the properties of the environment in the immediate vicinity of the MBH. As we will argue later in this paper, *existing* MBH spin measurements allow for testing and placing constraints on this conjectured link. The basic assumption behind our attempt is that the mechanism fueling the MBH—either disk instabilities or galaxy mergers—bridges large and small scales, ensuring that the degree of “disorder” of each galactic component (gas and stars) does not change much from galactic to circumnuclear scales. At kiloparsec scales, a routinely observed measure of “disorder” is the v/σ ratio, where v is the bulk rotation velocity of the system, and σ is its velocity dispersion. Therefore, the remaining issue is whether the gas that is brought down to the MBH and *gets accreted* has a v/σ more similar to that of the surrounding stars in the bulge or to that of the gas in the galactic disk. In the absence of solid theoretical predictions and observational evidence, we explore a few models, further differentiating between elliptical and spiral galaxies. As a consequence, we are able to predict different spin evolution in different galaxy types, which allows us to constrain our models (and therefore the physics of the fueling mechanism) by comparing them to the observed MBH spin distribution in the local universe.

In the following, we first discuss observations of the v/σ ratio in galaxies (Section 3.1). These data will guide us in constructing models to assign a v/σ ratio to the accreting reservoir, according to the morphology of the host galaxy (Section 3.2). Finally, in Section 3.3 we will describe how to geometrically translate a given a value of the v/σ ratio for the reservoir into the isotropy parameter F used in the previous section to characterize the MBH spin evolution; see Equations (13) and (11).

¹⁰ The details of the alignment mechanism are, in any case, still a subject of debate; see, e.g., Sorathia et al. (2013a, 2013b) and references therein.

3.1. Measurements of v/σ

The ratio v/σ for the stellar and/or gaseous components of a galaxy has been measured for a variety of galaxy samples. We collected these data to construct v/σ distributions to implement in our galaxy evolution model. In the following we describe these measurements in detail, discriminating between gas measurements in galactic disks and stellar measurements in bulges.

3.1.1. Gaseous Disks

Measurements of v/σ for the gas component in spiral galaxies have been obtained with integral field emission line spectroscopy with subarcsec resolution, tracing the gas from 10 kpc down to subkiloparsec scales, depending on the redshift of the system. More specifically, Kassin et al. (2012) explicitly discuss the dependence of v/σ on redshift and stellar mass for disk galaxies at $z < 1.2$ using a sample of several hundred objects. Here, we complement their data with measurement at higher redshift. Wisnioski et al. (2011), Epinat et al. (2012), and Swinbank et al. (2012) report v/σ measurement for star-forming galaxies in the redshift range $1.2 < z < 1.7$; their data are combined in a catalog of 30 objects that we take as a representative sample at $z \approx 1.5$. Förster Schreiber et al. (2009), Law et al. (2009), and Newman et al. (2013) explore the range $1.5 < z < 2.5$; we combine their data in a catalog of 56 objects that we take as a representative sample at $z \approx 2$. Gnerucci et al. (2011) measure v/σ of 33 star-forming galaxies at high redshift, in the range $3 < z < 4.8$. They find a fraction of rotating systems (defined as systems having $v/\sigma > 1$) of $\sim 1/3$, claiming that “the comparison between the SINS analysis at $z \sim 2$ and the AMAZE analysis at $z \sim 3.3$ suggests that the fraction of rotating objects does not evolve within this redshift interval” (Gnerucci et al. 2011, p. 19). Unfortunately, they do not provide a full set of mass and v/σ measurements for all the objects in their sample. For fitting purposes, we then just assume another set of measurements at $z \sim 3.3$, mirroring the ones at $z \approx 2$. Each data sample is divided into galaxy stellar mass (M_*) bins, and for each mass bin we compute the mean v/σ and the dispersion around the mean. We therefore end up with a series of measurements of v/σ in the z - M_* plane, which we then fit with a “Nuker’s law” of the form

$$\frac{v}{\sigma} = a \left(\frac{x}{x_0} \right)^\alpha \left[1 + \left(\frac{x}{x_0} \right)^\beta \right]^{-\alpha/\beta}, \quad (14)$$

where $x = \log(1+z)$, and $x_0 = b(\log M_* + c)$.

Equation (14) describes a broken power law where the slope at $x > x_0$ is forced to zero and the location of the break, x_0 , depends on the stellar mass of the system. The parameter β describes the “sharpness” of the transition between the two power laws. The best least-square fit to the data gives the following values for the five parameters: $a = 0.6949$; $b = 0.4548$; $c = -8.5255$; $\alpha = -0.8680$; and $\beta = 3.2126$.¹¹ Data and best fit are shown in Figure 4. To account for the data dispersion around the best fit, we assume that the density distribution for v/σ is log-normal with standard deviation of 0.34 dex around Equation (14).

¹¹ Note that the fitting function (14) becomes singular for low stellar masses $\log M_* < c$. For those masses, we simply assume $v/\sigma \approx 1$. We stress that this simplifying assumption has a negligible impact on our results, as such low stellar masses are only frequent at high redshifts and for galaxies hosting small MBHs with mass $M_{\text{bh}} \lesssim 10^6 M_\odot$. For such small MBHs, as will be clear later in this paper, the Bardeen–Petterson effect makes accretion effectively coherent, irrespective of the v/σ ratio.

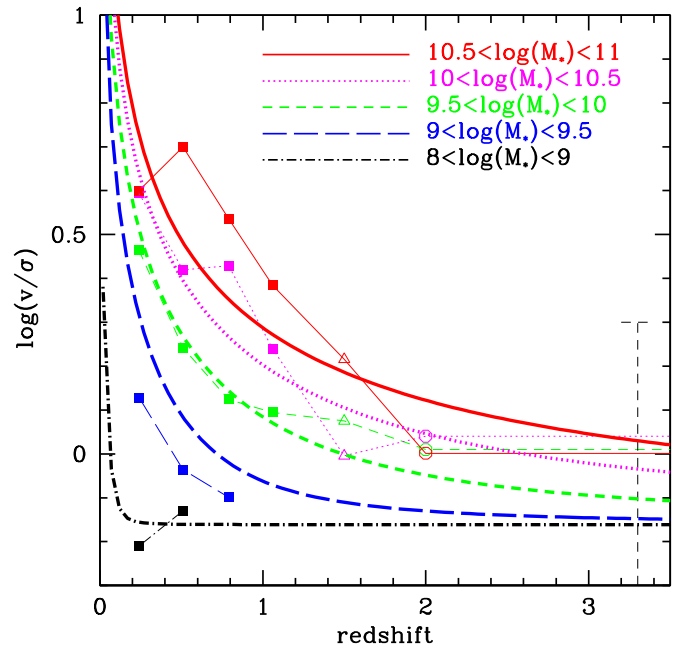


Figure 4. v/σ of gas on kiloparsec scales in gas-rich galaxies. Points are derived from the literature: filled squares are derived from Kassin et al. (2012), whereas open triangles and open circles are derived from the $z \approx 1.5$ and $z \approx 2$ samples, respectively. Data sets have been grouped and binned as described in the main text. The dashed vertical line at $z = 3.3$ marks the v/σ range reported by Gnerucci et al. (2011). Different colors and line styles correspond to different mass bins, as labeled in the figure. Smooth thick lines represent the best fit to the data given by Equation (14), evaluated at the middle point of each $\log M_*$ bin. The average dispersion of the measurement of each data point is ≈ 0.34 dex in $\log(v/\sigma)$.

(A color version of this figure is available in the online journal.)

3.1.2. In Stellar Bulges

The kinematics of stellar bulges has also been extensively studied in the literature. The SAURON project (Cappellari et al. 2007) focuses on a sample of 48 ellipticals and lenticular galaxies, completed with 18 objects from the literature, for a total of 66 objects. Kinematic measurements are also available for stellar bulges of spiral galaxies; Fabricius et al. (2012) report measurements of v/σ for bulges in 43 spiral galaxies of all classes, from S0 to Sc, also making a distinction between bulges and “pseudobulges.” Using the total sample of 109 objects, we note that, in general, a distinction can be made between ellipticals and lenticular/spirals. The former have lower v/σ , clustering at zero values, whereas the latter have generally higher v/σ , extending to values greater than 1 and with an average greater than 0.5. Moreover, “pseudobulge” spirals tend to rotate faster than classical bulges, as shown in Figure 5. The v/σ distribution is analytically fitted with the following functions:

1. ellipticals

$$f(x) = ae^{bx^c}, \quad (15)$$

with $a = 14.59$, $b = -3.98$, $c = 0.96$;

2. bulges and pseudobulges in spirals

$$f(x) = ax^b e^{cx^d}, \quad (16)$$

with $a = 42.24$, $b = 1.29$, $c = -2.95$, $d = 2.81$;

3. bulges in spirals

$$f(x) = \frac{a}{b} x^b e^{-0.5[(x-c)/b]^2}, \quad (17)$$

with $a = 2.10$, $b = 0.24$, $c = 0.47$; and

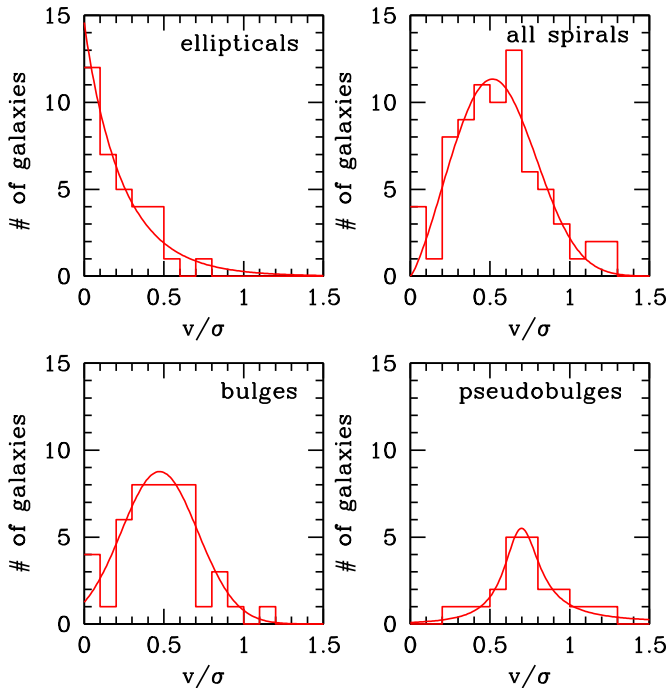


Figure 5. Distribution of v/σ for different galaxy types (as labeled in the panels) at low redshifts. In each panel, the red histogram is the distribution of observed v/σ , and the overlaid curve is the analytical fit reported in the main text.

(A color version of this figure is available in the online journal.)

4. pseudobulges in spirals

$$f(x) = \frac{a(x-b)}{x^2 + cx + d}, \quad (18)$$

with $a = 0.083$, $b = -0.53$, $c = -1.38$, $d = 0.50$.

The distribution of v/σ for the different galaxy samples, together with the corresponding $f(x)$ fitting formulae given by Equations (15)–(18), is shown in Figure 5. When implemented in our code, we normalize each $f(x)$ so that $\int_0^\infty f(x)dx = 1$ to get a probability density function (PDF). The v/σ of each individual galaxy is then drawn randomly from the appropriate PDF according to its morphological type, as described in detail in the next section.

3.2. Implementation in Our Galaxy Formation Model

Following what is usually done in semianalytic models (see, e.g., Guo et al. 2011; Wilman et al. 2013; Bonoli et al. 2014), we define ellipticals as those galaxies with a bulge-to-total-mass ratio $B/T > 0.7$ and spirals as the remaining galaxies (i.e., $B/T < 0.7$).

Since in *ellipticals* (in particular the most massive ones at lower redshifts) cold gas is subdominant, we always assume that in these galaxies the dynamics of the gas feeding the MBH traces that of the stellar population, and we thus extract v/σ from the observational distribution given by Equation (15) for ellipticals.

Fueling of the MBH in *spiral galaxies* might be more subtle. We therefore explore three different models that encompass plausible scenarios.

1. *Pseudobulge model.* Stars in the bulge are formed out of the same galactic flow that simultaneously replenishes the gas reservoir available to accrete on the MBH. Therefore, one may conjecture that this common origin should imply

a similar velocity dispersion. This may happen if the dissipation (through shocks) in the gas of the reservoir acts on a longer timescale than accretion. In our model, spiral bulges form either via disk instabilities or via mergers. In the former case, we assume that a pseudobulge forms, assigning the reservoir a v/σ ratio drawn from the distribution given in Equation (18) for pseudobulges hosted in spirals; in the latter case we assume that a classical bulge forms, extracting v/σ from the observational distribution given in Equation (17) for classical bulges hosted in spirals. The assigned value of v/σ is then kept constant during the galaxy’s evolution, as long as the morphology does not change. In our model, morphology changes can be triggered by disk instabilities or major mergers. Thus, whenever one such event changes the galaxy morphology, we reset the value of v/σ according to the PDFs above. In the case of minor mergers, instead, galactic disks are usually not disrupted, preserving the galaxy morphology. Hence, we simply take the v/σ of the resulting galaxy to be the average of the v/σ of the progenitors, weighed with their respective baryonic masses. In practice, the resulting v/σ is always much closer to that of the more massive progenitor.¹²

2. *Disk model.* The gas fueling the MBH comes from kiloparsec scales. An alternative model can thus be envisaged where the low-angular-momentum reservoir accreting onto the MBH shares the kinematic properties of the large-scale gaseous disk. This is because one may conjecture that gaseous disks at all scales should be affected by major mergers and/or bar instabilities in similar ways, when such events occur. To apply this scenario, we need to extract, for each spiral galaxy, a v/σ ratio from a log-normal distribution with average given by Equation (14) and standard deviation of 0.34 dex. However, tracking the cosmic evolution of MBH spins in this model is slightly more complex than in the *pseudobulge* model, because the typical v/σ of the large-scale disk in spirals depends explicitly on the stellar mass M_* and on z (see Equation (14)), unlike what happens for ellipticals (see Equation (15)). This calls for a different implementation of the velocity dispersion evolution in ellipticals and in spirals. More specifically, when a galaxy has $B/T > 0.7$, we assign it a v/σ ratio from the observational distribution given by Equation (15) for ellipticals and keep it constant until a disk instability or a major merger changes the morphology. When $B/T < 0.7$, we assign the galaxy an “intrinsic dispersion” χ relative to the typical value given by Equation (14). More precisely, we draw χ from a normal distribution with zero average and standard deviation 0.34 and then relate the galaxy’s v/σ to this intrinsic dispersion via $\log(v/\sigma) = \log(v/\sigma)|_{\text{av}}(M_*, z) + \chi$, where $(v/\sigma)|_{\text{av}}(M_*, z)$ is the value of the observational fit given by Equation (14) for gas in spirals. This procedure thus assigns the galaxy a v/σ ratio drawn from a log-normal distribution with average given by Equation (14) and dispersion 0.34 dex. The intrinsic dispersion χ is then kept constant along the quiescent galaxy evolution phase, while $(v/\sigma)|_{\text{av}}(M_*, z)$ evolves as M_* and z change. When a morphology change (following a major merger or a disk instability) occurs we reset the value of v/σ based on the PDF that is appropriate, as dictated by the new galaxy morphology, while at minor mergers we combine the v/σ ratios in a weighed average as in the *pseudobulge* model.

¹² We refer the reader to B12 for more detail on the definition and implementation of minor/major mergers and disk instabilities.

3. *Hybrid model.* This model is intermediate between the *disk* and the *pseudobulge* models because in the case of classical bulges it relates the MBH fueling in spirals to the stellar bulge kinematics, while in the case of pseudobulges the MBH fueling is linked to the kinematics of the large-scale gaseous disk. The motivation is a possible different origin for the gas reservoir in the two cases. The gas accreting on the MBH in pseudobulges may be more likely to retain a certain degree of coherence, because it originated from a bar instability. This residual coherence may be larger than in the stellar component because unlike gas, stars do not dissipate random motions through shocks. In the case of classical bulges, we thus extract v/σ from the observational distribution given in Equation (16) for all spirals,¹³ while for pseudobulges we assume, as in model (2), a log-normal distribution with average given by Equation (14) and standard deviation of 0.34 dex. The evolution of the v/σ ratios for the accreting reservoir is tracked using the (combined) techniques applied in models (1) and (2).

For the sake of comparison, we also investigate three more idealized models for accretion onto the MBH that are often adopted in the literature, namely, a purely coherent accretion scenario (where accretion always takes place on a prograde accretion disk orthogonal to the MBH spin) and two variants of a purely chaotic accretion scenario (where the accreting gas has a perfectly isotropic angular momentum distribution). We postpone a detailed description of these models and their implementation to Appendix B.

For each of the accretion models that we consider, we perform two sets of runs seeding MBHs either as Pop III remnants at $z \sim 20$ (*light seeds*) or as the end product of direct collapse at $z \sim 15$ (*heavy seeds*); see B12 for more details. Each run consists of $\sim 24,000$ merger trees¹⁴ in the dark-matter halo mass range 10^{10} – $10^{15} M_{\odot}$. In this paper we focus on MBHs of $M_{\text{bh}} > 10^6 M_{\odot}$ at relatively low z , because we aim at a comparison with measured spins in the local universe. Since memory of the seeding process already fades away at high redshift, we did not find any significant difference between the light- and heavy-seed prescriptions at any considered redshift for any considered galaxy subsample. We therefore add up light- and heavy-seed runs to increase the statistics and “smoothness” of our theoretical samples to be compared with the observed data (see Section 6.2).

3.3. Linking v/σ to the Isotropy Parameter F

When the dispersion of the low-angular-momentum reservoir available for accretion is known, one can compute the amount of prograde/retrograde accretion and derive the MBH spin evolution (see Section 2.2). The relation between the v/σ ratio of the accretion flow and the geometrical parameter F introduced earlier to describe the anisotropy of the angular momentum distribution of the accreting clouds can be derived as follows. Suppose that the net rotation is along the z axis. Each lump of matter falling into the MBH has an angular momentum with z -component $L_z = mr \sin(\theta + \sigma_{\varphi})$, where θ and φ are the lump’s polar and azimuthal angles in a spherical coordinate

¹³ The observational distributions for classical bulges in spirals (Equation (17)) or for pseudobulges in spirals (Equation (18)) yield analog results, but the combined distribution given by Equation (16) has better statistics because it is based on a larger sample.

¹⁴ For the coherent/chaotic models we perform shorter runs with a factor of 20 fewer halos.

Table 1
The Calibrated Values of the Free Parameters of the Model
(See B12 and Section 2.2 for Their Meaning)

	Light Seeds	Heavy Seeds
M_{cloud}	$3 \times 10^4 M_{\odot}$	$3 \times 10^4 M_{\odot}$
$\epsilon_{\text{SN,b}}$	0.4	0.4
$\epsilon_{\text{SN,d}}$	0.1	0.1
f_{jet}	10	10
A_{res}	6×10^{-3}	5.75×10^{-3}
A_{Edd}	2.2	1
k_{accr}	10^{-3}	10^{-3}

system, and σ_{φ} is the projection of σ on the tangential direction \mathbf{e}_{φ} . Let us now write $\sigma_{\varphi} = \sigma \cos \alpha$, where α is the angle between σ and \mathbf{e}_{φ} . If σ is isotropically distributed, $\cos \alpha$ has a uniform probability distribution, i.e., $dP/d\cos \alpha = 1/2$. If $v/\sigma > 1$, L_z is always positive and $F = 1$. If $0 \leq v/\sigma < 1$, the probability of having $L_z > 0$ (or $L_z < 0$) is proportional to $1 + v/\sigma$ (or $1 - v/\sigma$), hence $F = (1 + v/\sigma)/2$. In summary, we assume

$$\begin{aligned} v/\sigma > 1 &\rightarrow F = 1; \\ v/\sigma = 0 &\rightarrow F = 0.5; \\ 0 < v/\sigma < 1 &\rightarrow F = (1 + v/\sigma)/2. \end{aligned} \quad (19)$$

One subtlety should be noted about Equation (19) and its derivation. When using the parameter F resulting from this equation in Equation (13), one is implicitly identifying the reference system used above to derive Equation (19) (i.e., one where the z axis is along the total angular momentum of the gas reservoir, out of which the accreting lumps are drawn) with the reference system used to derive Equation (13) (i.e., one where the polar angle θ_{out} is defined relative to a z axis parallel to the MBH spin). Therefore, we are implicitly assuming that the MBH spin is exactly aligned with the average angular momentum of the clouds already when the *first* cloud hits the MBH. This may not be the case under many circumstances, but the impact of this assumption on our predictions for the MBH spin *magnitudes* is expected to be small for the following two reasons: (1) When the MBH is light enough ($M_{\text{bh}} \lesssim 10^7 M_{\odot}$) to be in the $J_{\text{disk}}/2J_{\text{bh}} > 1$ regime, the MBH spin realigns with each cloud-angular momentum on a timescale shorter than the accretion time. Therefore, assuming the MBH spin to be always aligned with the clouds average rotation axis does not significantly affect the evolution of the spin *magnitude*. (2) The high-mass regime of our model is exact for the two limiting cases $F = 0.5$ and $F = 1$ and also preserves the correct monotonic trend for $0.5 < F < 1$ (i.e., the higher F , the higher the MBH spin magnitude). It would indeed be possible to estimate the detailed effect of the initial MBH orientation for $0.5 < F < 1$ by comparing Figure 3 with Figures 6 and 7 in D13 for $M_{\text{bh}} \gtrsim 10^9 M_{\odot}$, but we postpone a more detailed analysis to a future work.

4. CALIBRATION AGAINST OBSERVABLES

As in B12, we anchor our model to a number of observables, with particular attention to quantities characterizing the MBH population and their accretion properties in the local $z \sim 0$ universe, where all the currently available MBH spin measurements are performed.

More precisely, we calibrate our free parameters (see Table 1) against observational data for the QSO luminosity function at $z = 0.1$ (Figure 6), the MBH mass function at $z = 0$ (Figure 7), the local “Magorrian” relation between the MBH mass and the

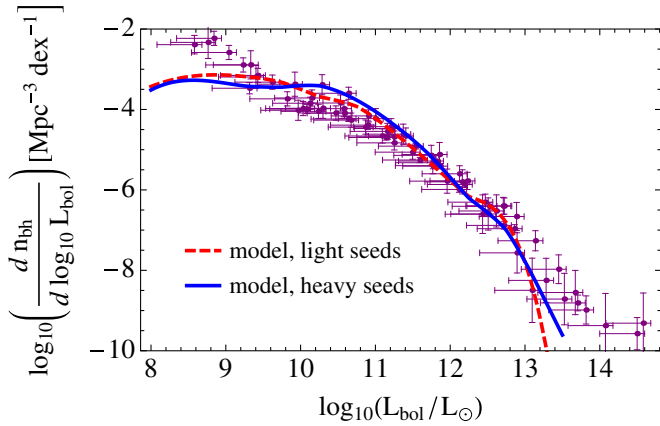


Figure 6. MBH bolometric luminosity function at $z = 0.1$ predicted by our model vs. the compilation of observational data by Hopkins et al. (2007). The vertical error bars on the data are from Hopkins et al. (2007), while for the horizontal ones we have assumed -0.5 dex and $+0.1$ dex to account for possible overestimation of the bolometric correction (Lusso et al. 2012).

(A color version of this figure is available in the online journal.)

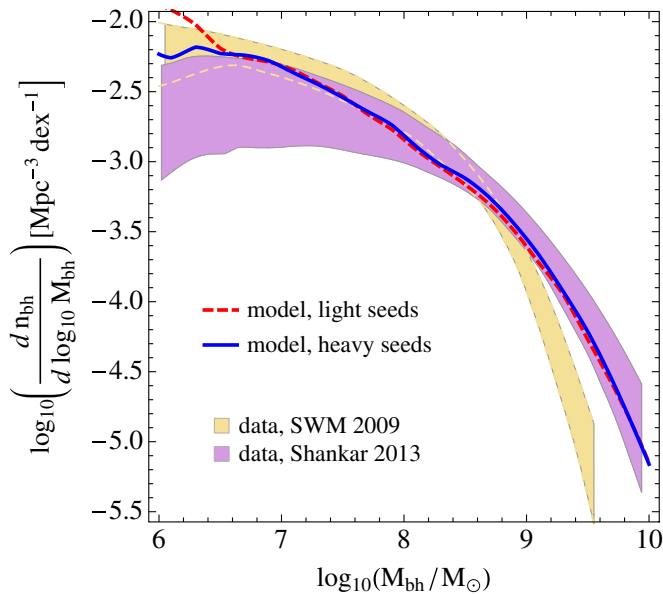


Figure 7. MBH mass function at $z = 0.1$ predicted by our model vs. the ranges, reconstructed from observational data, given by Shankar et al. (2009) and Shankar (2013). Note that although the results of Shankar (2013) are still preliminary and are based only on bulge-dominated galaxies, it is clear that systematic errors still dominate the uncertainties in the high-mass end.

(A color version of this figure is available in the online journal.)

bulge dynamical mass in ellipticals (Figure 8), the star formation density for $0 \leq z \lesssim 5$ (Figure 9), the stellar mass function at $z = 0$ (Figure 10), and the observed fraction of galaxies with given morphology at $z = 0$ (Figure 11). We stress, however, that the results of our model (and the overall conclusions of this paper) do not depend strongly on the values of these free parameters. Also, the results shown in this section are for the *pseudobulge* model (see Section 3.2), but the *disk* and *hybrid* models produce similar results.

As can be seen from Figure 6, our model gives reasonable predictions for the $z = 0.1$ QSO luminosity function when compared to the compilation of observational data by Hopkins et al. (2007), despite slightly underestimating it at low luminosities (the disagreement at the high-luminosity end is less statistically significant). The vertical error bars on the data are

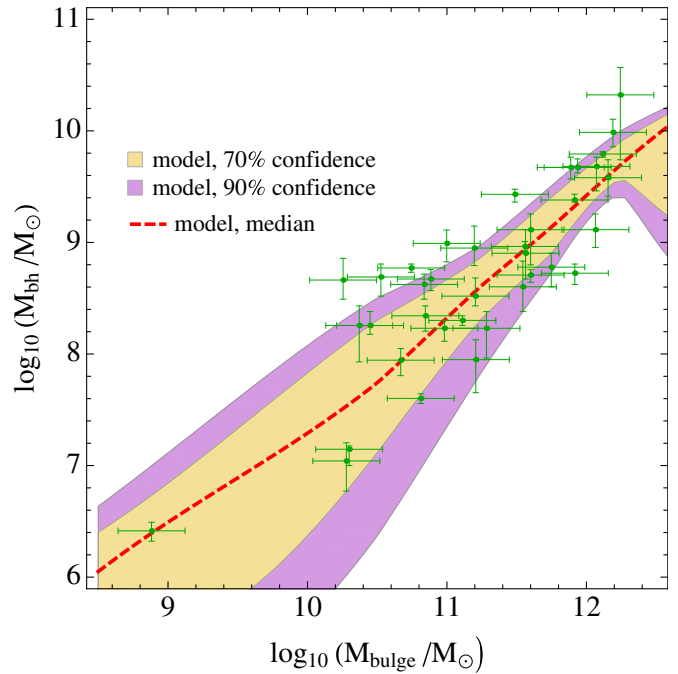


Figure 8. Relation between the MBH mass and the dynamical mass of the bulge predicted by our model at $z = 0$, compared to the data compilation of McConnell & Ma (2013). This figure adopts a light-seed model, but the heavy-seed model leads to similar results.

(A color version of this figure is available in the online journal.)

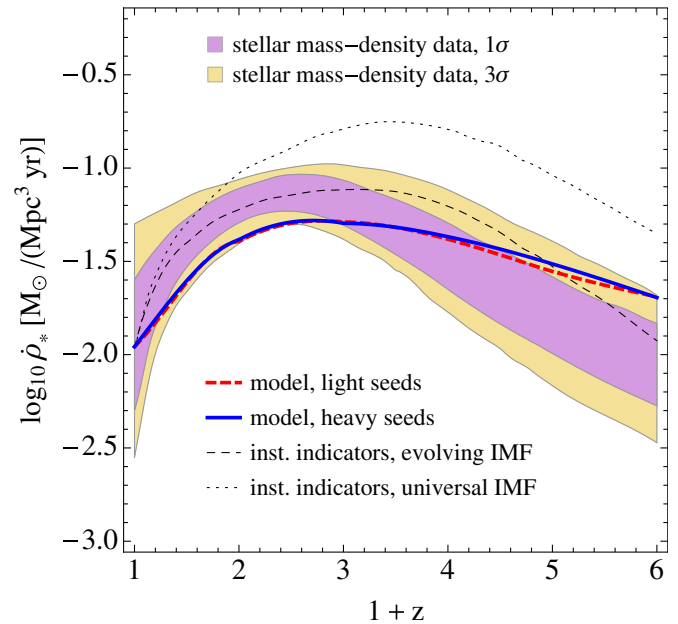


Figure 9. Star formation density as a function of redshift, as predicted by our model vs. the one derived by Wilkins et al. (2008) from observations of the stellar mass density and assuming an evolving IMF (shaded regions, corresponding to 1σ and 3σ confidence regions). We also show fits to instantaneous star formation density indicators, assuming either a universal or an evolving IMF (Wilkins et al. 2008).

(A color version of this figure is available in the online journal.)

from Hopkins et al. (2007), while for the horizontal ones we have assumed -0.5 dex and $+0.1$ dex to account for possible overestimation of the bolometric correction (Lusso et al. 2012). Similarly, Figure 7 shows that our predictions for the $z = 0$ black hole mass function are in agreement with recent estimates

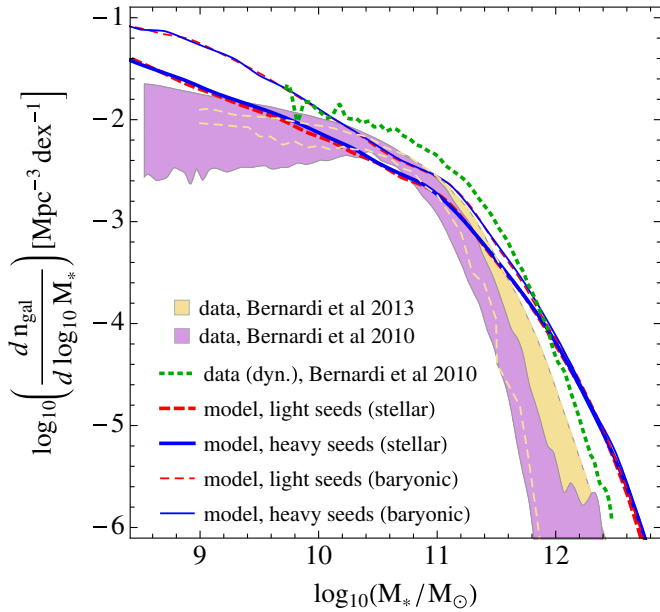


Figure 10. Mass function of galaxies at $z = 0$ predicted by our model (including the stellar mass alone or the total baryonic mass in gas and stars) vs. the estimates of Bernardi et al. (2010) and Bernardi et al. (2013) for the stellar mass function from luminosity observations and the estimate of Bernardi et al. (2010) for the dynamical mass function (obtained by reconstructing the dynamical masses through the galaxy’s size and velocity dispersion).

(A color version of this figure is available in the online journal.)

by Shankar (2013). While the reconstruction of the MBH mass function performed by Shankar (2013) is still preliminary and based only on bulge-dominated galaxies, from a comparison to the observational estimates of Shankar et al. (2009; also shown in Figure 7), it is clear that systematic errors still dominate the determination of the mass function at the high-mass end and that our model’s prediction is clearly within the observational uncertainties. Figure 8 shows the agreement between a compilation of dynamical bulge masses and black hole masses in elliptical galaxies from McConnell & Ma (2013; see also Häring & Rix 2004; Magorrian et al. 1998) and our predictions for ellipticals.

The improved star formation implementation described in Section 2.1 allows our model to better reproduce data for the star formation history than the original prescription of B12. Figure 9 compares our predictions to reconstructions based either on observations of the stellar mass density and assuming an evolving initial mass function (IMF; Wilkins et al. 2008) or to fits to instantaneous star formation density observations, assuming either a universal or an evolving IMF (Wilkins et al. 2008). Our predictions for the local galaxy mass function (Figure 10) are instead slightly higher than the observational determinations by Bernardi et al. (2010, 2013) at the low- and high-mass ends. The same problem is often seen in galaxy formation models, which tend to overproduce stars (see, e.g., De Lucia & Blaizot 2007; Guo et al. 2011; Khandai et al. 2014), possibly because of overly simplified treatments of AGNs and supernova feedback. More sophisticated feedback schemes might improve the match with observations, and we plan to investigate this issue further in future work. However, one should also keep in mind that determinations of the mass function are typically obtained by estimating galaxy masses through their luminosity, which results in large systematic uncertainties (especially at the high-mass end), due to the assumptions on the stellar mass-to-light ratio, as well as the different possible ways in which one

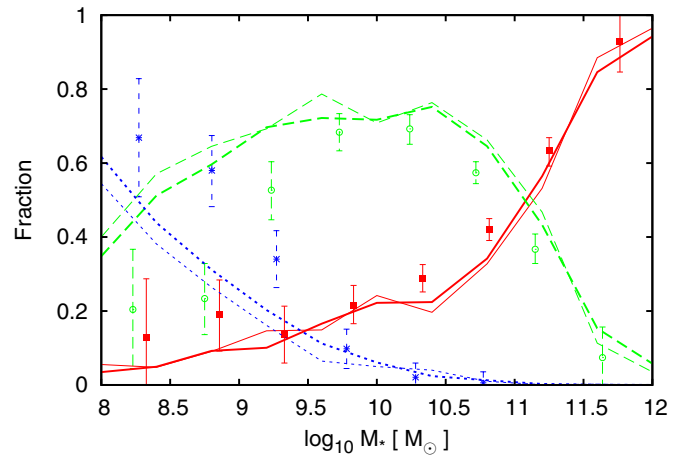


Figure 11. Morphologies predicted by our model at $z = 0$ as a function of the stellar mass (thick lines, heavy seeds; thin lines, light seeds) vs. data from Conscience (2006) (squares, ellipticals; circles, spirals; stars, irregulars).

(A color version of this figure is available in the online journal.)

can fit the light profiles (Bernardi et al. 2013). Finally, Figure 11 shows the predicted fraction of ellipticals, spirals, and irregulars as a function of stellar mass, together with the observational estimates of Conscience (2006). More specifically, following Guo et al. (2011), we use the fraction of total baryonic mass in the bulge, $B/T = M_b/(M_b + M_d)$ (with M_b and M_d the bulge and disk masses), to discriminate the various morphologies; that is, we classify a galaxy as an elliptical when $B/T > 0.7$, as a spiral when $0.03 < B/T < 0.7$, and as an irregular when $B/T < 0.03$.¹⁵ In spite of this simplistic classification, our model reproduces, at least qualitatively, the observational results. Because in Section 6 we will be dealing with accreting systems, in Figure 12 we compare the Eddington ratio, f_{Edd} , distribution predicted by our model to observations. In the top panel, we compare the local cumulative distribution of f_{Edd} as measured by Heckman et al. (2004), who inspected 23,000 active galaxies in a complete sample of 123,000 galaxies from the Sloan Digital Sky Survey in the redshift range $0.05 < z < 0.2$ to the predictions of our *pseudobulge* model at $z = 0.1$ (other models yield similar results). The model reproduces the f_{Edd} observed trend satisfactorily, even though it slightly underpredicts the fraction of accreting systems at $f_{\text{Edd}} > 0.01$. The lower panels highlight the difference between the model and the data at $f_{\text{Edd}} \approx 0.1$. The figure shows that our model catches the main trends in the low-redshift Eddington ratio distributions, although not perfectly. A better calibration of the model against this quantity may be considered in future work.

5. MBH SPIN EVOLUTION

The spin evolution of each MBH is dictated by a complex interplay of (1) the variable supply of mass available for accretion, (2) the time-changing host galaxy properties and morphology, and (3) MBH binary coalescence events. We will first inspect some examples of individual MBH–galaxy evolutionary tracks to illustrate the effect of those ingredients (Section 5.1). We stress that the few examples we consider do not represent the whole variety of evolutionary paths predicted

¹⁵ Qualitatively similar results are obtained using stellar rather than total baryonic masses to define B/T , but it seems preferable to use total baryonic masses if one wants to apply the same classification to high redshifts, where gas may dominate over stars.

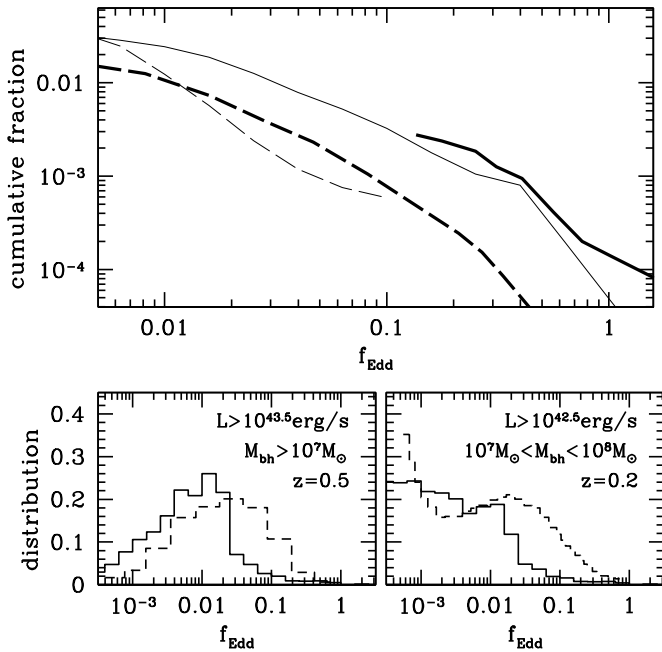


Figure 12. Distribution of Eddington ratios f_{Edd} . In the top panel the cumulative fraction of MBHs accreting above a certain Eddington ratio is shown for two different MBH mass bins. Thin lines show the predictions of our model at $z = 0.1$ for the mass bins $2 \times 10^6 M_{\odot} < M < 5 \times 10^6 M_{\odot}$ (solid) and $5 \times 10^7 M_{\odot} < M < 2 \times 10^8 M_{\odot}$ (long dashed). Those are compared with observational estimates from Heckman et al. (2004) (thick lines) evaluated at $M_{\text{bh}} = 3 \times 10^6 M_{\odot}$ (solid) and $M_{\text{bh}} = 10^8 M_{\odot}$ (long dashed). In the bottom panels, the f_{Edd} distributions for selected systems (as labeled in each panel) are compared to data from Hickox et al. (2009; left) and Kauffmann & Heckman (2009; right). Solid histograms are the predictions of our model, while dashed histograms are the data.

by our model. Predictions on statistically significant samples of objects will be presented in Section 5.2.

5.1. Spin Evolution of Individual MBHs

Figure 13 gives three examples of evolution of $z = 0$ spirals for the *pseudobulge* model. More specifically, we show the evolution of the MBH mass (with MBH mergers shown with filled circles) along the main MBH progenitor history (i.e., at each MBH merger we follow the more massive progenitor back in time). Also shown are the MBH spin, the mass of the reservoir available for accretion onto the MBH, as well as the host galaxy morphology (with the redshift intervals in which the galaxy is elliptical, i.e., $B/T > 0.7$, marked by a lavender-shaded area).

The two right panels show two MBHs accreting at $f_{\text{Edd}} \approx 1.6 \times 10^{-2}$ at $z \approx 0$. Despite the similarity of the accretion rates and galaxy morphologies at $z \approx 0$, the final MBH spins are quite different. In both cases, the spin grows rapidly early on and remains almost maximal as long as the MBH mass is $\lesssim 10^6 M_{\odot}$. This is because, as discussed earlier, for such low masses the MBH spin is smaller than the typical angular momentum of the accretion disk arising from the capture of a cloud, and as a result the Bardeen–Petterson effect aligns the MBH spin to the disk’s angular momentum, thus making accretion effectively coherent. However, the later evolution of the two cases is quite different and reflects the wide kinematic range of bulges and pseudobulges shown in Figure 5, with v/σ above (below) 1 resulting in high (moderate) MBH spins. For instance, in the bottom right panel the spin first drops to ≈ 0.25 and then rises again to ≈ 0.8 following a series of MBH mergers and accretion

events (triggered by disk instabilities and major mergers). A major galactic merger at $z \approx 0$ then triggers a MBH merger and an accretion event that result in a final spin ≈ 0.75 . In the top right panel, instead, accretion and mergers also cause the spin to drop to ≈ 0.4 at $z \approx 4$, but the degree of anisotropy of the MBH fueling (i.e., in the pseudobulge model, the value of v/σ of the host galaxy’s stellar population) is never large enough to allow for very large spins in the subsequent evolution. In the left panel, we show a highly sub-Eddington system, which has a final MBH spin of ≈ 0.5 . In this case, a major merger at $z \approx 2$ changes the morphology of the galaxy from spiral to elliptical, and the following highly “incoherent” (i.e., with $v/\sigma \ll 1$) accretion causes a dramatic spin down of the MBH. After that episode, the galaxy reacquires a substantial disk because of minor mergers and accretion/cooling of gas, thus becoming a spiral again, but the accretion rate onto the central MBH never becomes high enough to substantially change its spin.

These trends can be compared to those found in the *disk* model, shown in Figure 14. In the top right panel we consider a galaxy containing an accreting MBH with $M_{\text{bh}} \sim 10^6 M_{\odot}$ at $z = 0$. For such a small mass, the distinction between ellipticals and spirals and between the various accretion models (e.g., disk versus pseudobulge) is unimportant because the Bardeen–Petterson effect always aligns the MBH spin to the angular momentum of the incoming cloud. This makes accretion essentially coherent and results in almost maximal spins. The bottom left panel shows again an accreting MBH in a spiral galaxy, but with larger final mass ($M_{\text{bh}} \sim 10^8 M_{\odot}$ at $z = 0$). Again, accretion is effectively coherent (and the spin close to maximal) until the MBH grows larger than $\sim 10^6 M_{\odot}$. After that, the spin evolution during accretion events depends on the galaxy morphology. In particular, at $z \approx 2$ a major galactic merger (*not* accompanied by a MBH merger) triggers a morphology change to elliptical, as well as a QSO event that pushes the MBH spin to $a_{\text{bh}} \approx 0.3$. The galactic disk then regrows via minor mergers and accretion/cooling of gas, and accretion becomes “more coherent” (because the gas in spirals typically has $v/\sigma > 1$ at low redshift, see Figure 4). As a result, the MBH spin starts growing again, and at $z \approx 0$ an ongoing accretion event pushes it up to almost maximal values. The bottom right panel shows instead a nonaccreting (at $z \approx 0$) MBH hosted in an elliptical galaxy. Again, the spin remains close to maximal until $M_{\text{bh}} \sim 10^6 M_{\odot}$, after which the spin evolution is dominated by accretion, which tends to spin the MBH down when the host is elliptical (see the QSO event at $z \approx 2$). When the host is a spiral, instead, the spin tends to mildly grow during accretion events.

From the above examples we can draw a couple of conclusions. Nonaccreting systems (which we arbitrarily define as MBHs with $f_{\text{Edd}} < 0.01$) typically retain memory of the last “violent” event that changed the central MBH spin. Since this is likely to be a major merger/disk instability event that temporarily changes the galaxy morphology to bulge-dominated, the MBH spin will likely be small (nonmaximal, in any case), whether the galaxy later retains a bulge-like morphology or acquires a disk again. Highly accreting systems (i.e., with $f_{\text{Edd}} > 0.01$) will likely have their spin affected by the ongoing accretion episode. In this case, the spin at $z = 0$ depends on the typical v/σ ratio of the host galaxy. Spirals in the *pseudobulge* model have a range of possible spins mirroring the wide spread in v/σ . Conversely, spirals in the *disk* model are almost certain to have nearly maximally spinning MBHs. On the other hand, MBHs in accreting ellipticals tend to have low spins, because of their typically low v/σ ratios, as shown in Figure 5.

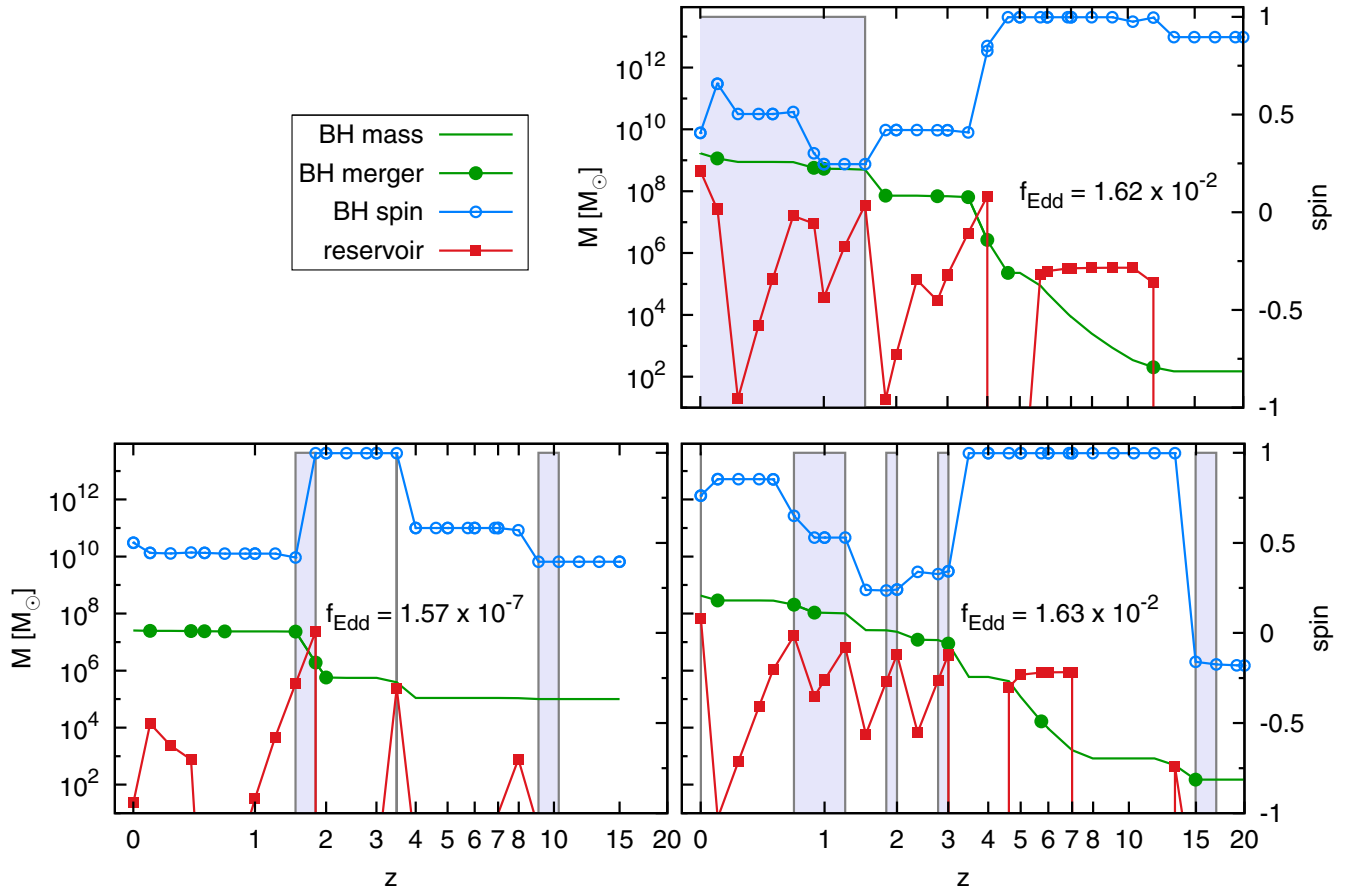


Figure 13. Examples of main-progenitor evolutionary tracks of three MBHs selected in the *pseudobulge* model. The MBH spin is represented by a blue solid line with empty circles; the mass of the MBH is represented by a solid green line (with filled circles representing the MBH mergers); and the reservoir mass is represented by solid lines with filled squares. The lavender-shaded areas indicate the redshifts at which the host is bulge-dominated ($B/T > 0.7$).

(A color version of this figure is available in the online journal.)

5.2. Spin Evolution of the Global MBH Population

Having discussed how accretion, mergers, and galaxy morphology contribute to the MBH spin buildup in individual galaxies, we now turn to the investigation of the cosmic spin evolution of the whole MBH population. In the three panels of Figure 15 we show the spin distributions predicted by the *pseudobulge* (top plot), *disk* (central plot), and *hybrid* (bottom plot) models for selected subsamples of galaxies at different redshifts.

As mentioned earlier, all three models adopt the same prescription for the spin evolution in elliptical galaxies (right column in each panel), which results in very similar distributions that do not evolve much from $z = 5$ to the present epoch. For $M_{\text{bh}} \lesssim 10^6 M_{\odot}$, $J_{\text{disk}}/2J_{\text{bh}} > 1$ and MBHs tend to have maximal spins. At large masses, $J_{\text{disk}}/2J_{\text{bh}} \ll 1$, and a_{bh} tends to the equilibrium value given by Figure 3. The median v/σ of elliptical galaxies is ≈ 0.2 , corresponding to $F \approx 0.6$, which translates to a median equilibrium spin of 0.3, in good agreement with Figure 15. The evolution of the overall population of spiral galaxies (central column) also shows similarities in all three models. This class of systems experiences more pronounced redshift evolution, and the median of the spin distribution shows a dip between $10^7 M_{\odot}$ and $10^8 M_{\odot}$ appearing at $z \sim 3$. The overall distributions are not very different from those of the ellipticals, but spins are on average larger by virtue of the typically higher v/σ , as shown in Figure 5.

The subset of *accreting* MBHs (i.e., with $f_{\text{Edd}} > 0.01$) in spirals (right column) shows instead a remarkably different

evolution between the *pseudobulge* and *disk* models. In the *pseudobulge* model, these galaxies maintain, on average, higher spins at all redshifts compared to other systems (see discussion in Section 5.1), but the trend of decreasing spin with increasing mass is preserved. Conversely, in the *disk* model, MBH spins show a stronger redshift evolution, and at $z < 2$ they tend to be maximal independently of the MBH mass. This is because MBHs are efficiently accreting gas with $v/\sigma > 1$ (see Figure 4). As expected, the *hybrid* model shows an evolution which is halfway between the *disk* and *pseudobulge* models.

Our predicted spin distributions are different for different classes of galaxies, which is a testable prediction. In general, MBHs in *ellipticals* have lower spins than their spiral counterparts, but still with an average value of $a_{\text{bh}} \approx 0.4$ and a long tail extending to much higher values. We note that our findings do not rule out spin-powered jet models (see, e.g., Sikora et al. 2007). Indeed, in such models the power of the jet is usually $\propto a_{\text{bh}}^2$ (Blandford & Znajek 1977; Tchekhovskoy et al. 2010; Narayan et al. 2014), implying a difference of just a factor of a few in luminosity between maximally and mildly spinning MBHs. It is also clear that in our model, accreting MBHs tend to be biased toward higher spins than nonaccreting ones, especially if located in spiral galaxies. In addition, current measurements of the MBH spins require large X-ray fluxes, which are only possible if the MBH shines at a significant fraction of the Eddington luminosity. Therefore, the current observed sample of MBH spins may not be an unbiased indicator of the overall cosmic MBH population. In the following we will perform a

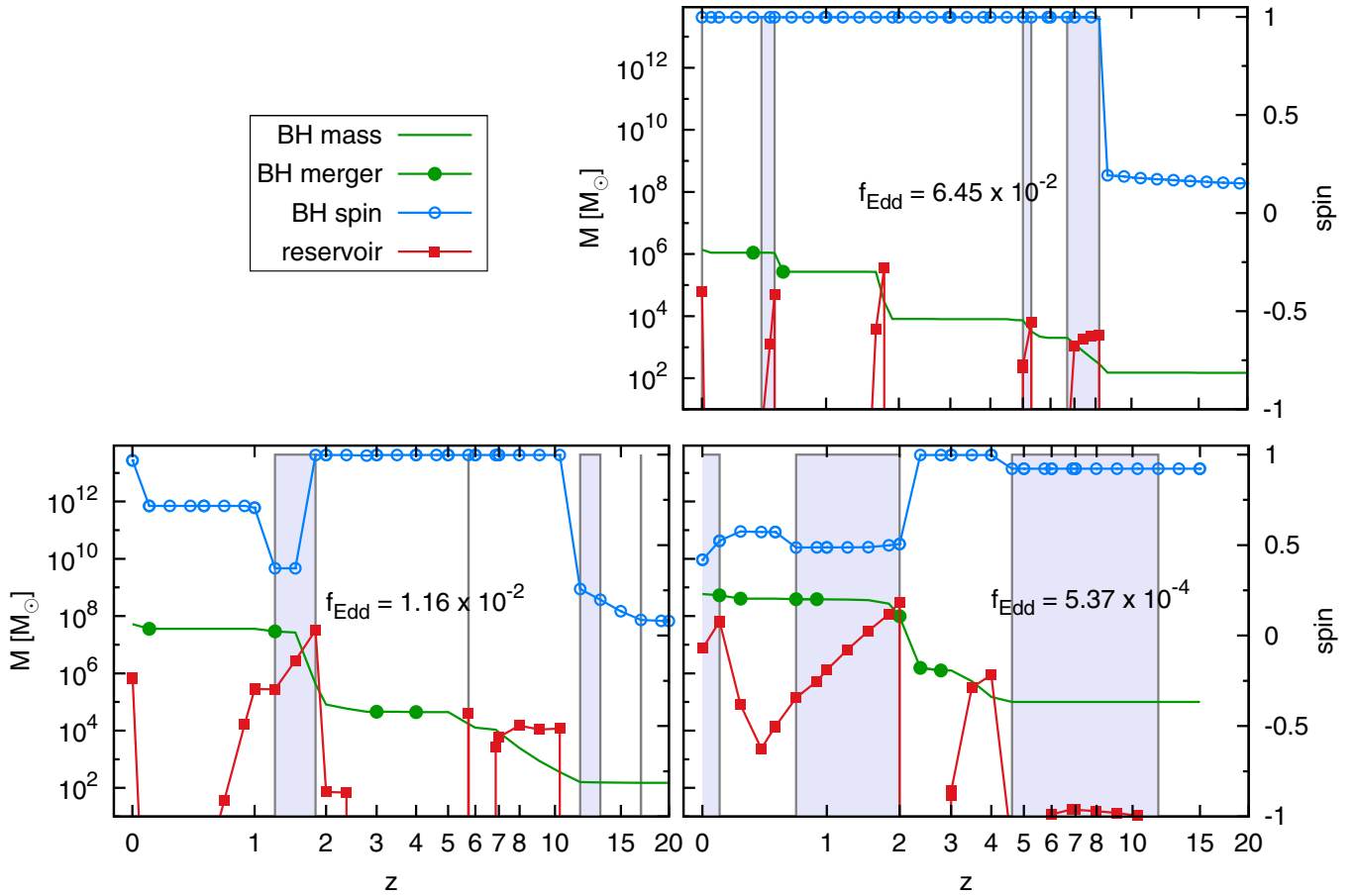


Figure 14. Same as Figure 13, but for the *disk* model.
(A color version of this figure is available in the online journal.)

statistical analysis comparing our predictions to the MBH spin measurements available today at $z < 0.1$, selecting the appropriate sample in our simulations in order to account for both these selection effects.

6. COMPARISON WITH OBSERVATIONS

We carry out here a quantitative comparison between MBH spin measurements and the output of our theoretical models, which link the MBH spin evolution to the properties of the galaxy host. However, existing spin measurements are sparse and are affected by several statistical and systematic uncertainties that are often difficult to quantify. The results of the following analysis should therefore be taken as indicative. Nonetheless, we will show that even with the current data, we can rule out some mass and spin growth scenarios and gain some qualitative insights about the connection between spin evolution and the properties of the galaxy host supplying gas to the accretion flow.

6.1. Observed Sample

MBH spins have been measured via $K\alpha$ reflection broad line modeling for about 20 objects. We took data from the sample compiled by Reynolds (2014), integrated with objects from Brenneman (2013). We noted some (minor) discrepancies in the numbers reported by the two authors; when necessary we inspected the original measurement papers (see references in Reynolds 2014 and Brenneman 2013) and obtained the values

directly from there. All the relevant properties of the sample are shown in Table 2. A meaningful comparison to a theoretical model is possible only if (1) observations have meaningful errors and (2) the general properties of the observed subsample can be isolated, and selection effects are understood. Both issues are somewhat tricky here.

Errors quoted in Table 2 represent the 68% confidence level in the mass and the 90% confidence level in the spin measurements. A complete knowledge of the PDF of those quantities would be desirable, but such information is often missing in the literature, and we can at best put forward educated guesses. For the (log of the) MBH mass, we consider (1) a Gaussian PDF with σ equal to the quoted error when the latter is symmetric with respect to the best measured value, (2) a flat PDF within the given errors when those are asymmetric, and (3) a Gaussian PDF with an arbitrary $\sigma = 0.3$ when errors are absent. Spin PDFs are instead derived by visually inspecting the function $\chi^2(a_{\text{bh}})$, which is always given in the relevant papers. We identify three families of measurements: (1) sometimes $\chi^2(a_{\text{bh}})$ has an approximately flat minimum, and in this case we take a flat PDF in the corresponding range; (2) for a few objects, $\chi^2(a_{\text{bh}})$ is extremely skewed on the left of the minimum, and in such cases we take as PDF the left half of a Gaussian distribution; (3) more often, $\chi^2(a_{\text{bh}})$ is quite symmetric (at least in the 99% confidence region), calling for a Gaussian model of the PDF. Details of the PDFs are given in the last column of Table 2. Being aware of the arbitrary nature of this procedure, we also consider an alternative model in which we take all errors in

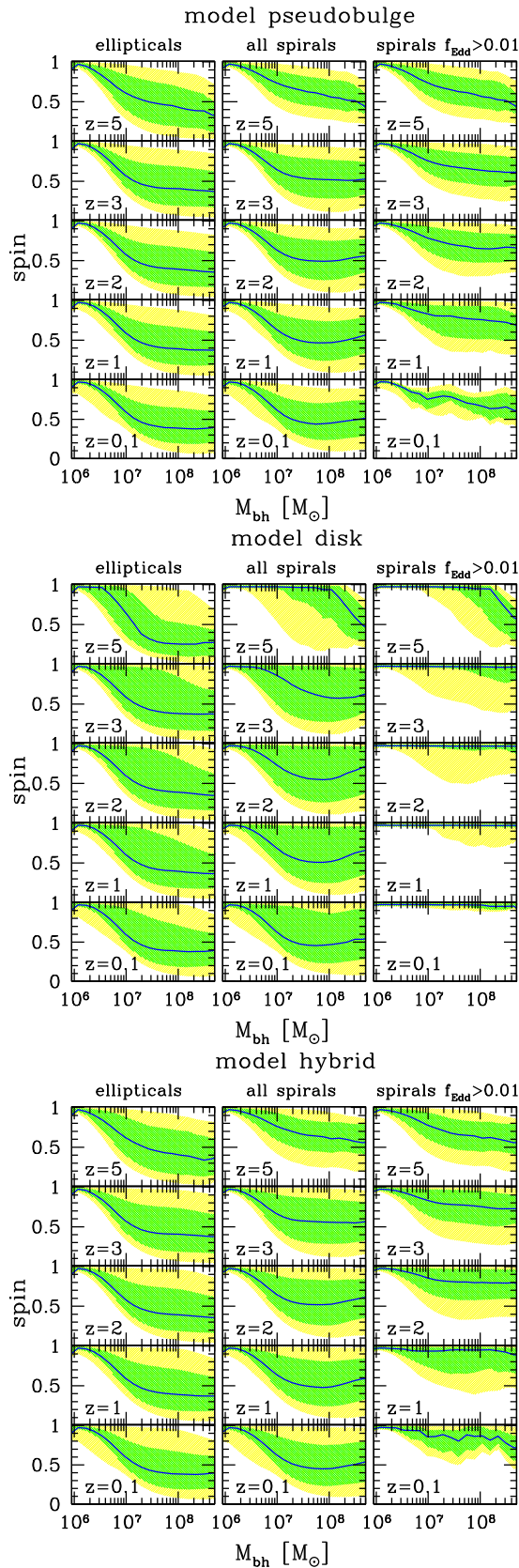


Figure 15. Spin evolution as a function of redshift for a different subsample of galaxies. The considered model is specified at the top of each panel. In each plot, the blue line is the median of the spin distribution as a function of the MBH mass and as predicted by the model, while green- and yellow-shaded areas represent the spin ranges enclosing 68% and 95% of the distribution. (A color version of this figure is available in the online journal.)

masses and spins to have a flat PDF within the range quoted in Column 7 of Table 2. We show in Appendix C that our results are largely independent of the adopted shape of the PDFs.

The obvious selection effect for a $K\alpha$ line measurement is that the source has to be bright in hard X (see also discussion in Brenneman et al. 2011); in fact, most of the MBHs in the sample reside in Seyfert 1 or narrow-line Seyfert 1 (NLS1) galaxies. Hosts are usually spirals or lenticular galaxies, with the exception of Mrk841. The observed sample is neither flux- nor volume-limited. X-ray luminosities and associated MBH masses have distributions consistent with being log-flat in the ranges 10^{42} – 10^{45} erg s $^{-1}$ and 10^6 – $3 \times 10^8 M_{\odot}$, respectively. Eddington ratios f_{Edd} are also evenly distributed in the range 0.01–1. The redshift distribution is also approximately flat in the range $0 < z < 0.07$, with two outliers at $z > 0.1$. Given these facts, the best-matching sample in our model is provided by spiral galaxies (defined by $B/T < 0.7$) with $f_{\text{Edd}} > 0.01$ at low redshift. For the purpose of the analysis, we will therefore exclude Mrk841 (which is an elliptical) and include all galaxies in the observed sample with unknown morphology (thus implicitly assuming they are spirals/lenticulars). Discarding the latter would weaken our results (because there would only be 12 objects in the observed sample) but not qualitatively change them.

6.2. Theoretical Sample

Theoretical distributions are computed with our model on a grid in the $M_{\text{bh}} - a_{\text{bh}}$ parameter space. The MBH mass range $10^6 M_{\odot} < M_{\text{bh}} < 5 \times 10^8 M_{\odot}$ is divided in five equally log-spaced bins, and for each bin, spin distributions are computed on 20 linear bins covering the range $0 < a_{\text{bh}} < 1$. We applied Gaussian kernel smoothing to each measured spin with $\sigma = 0.05$ to get smoother distributions¹⁶. To check the robustness of our results against spin binning, we also constructed two theoretical distributions using 10 and 30 linear a_{bh} bins and one distribution considering 20 bins both in log mass and spin. As a sanity check, a comparison among the results obtained with different binning choices is performed in Appendix C.

As mentioned above, all (but one) MBHs with spin measurements are accreting at $f_{\text{Edd}} > 0.01$ and reside in spiral or lenticular galaxies at $z < 0.1$. Those systems, although present in fair number, are necessarily rare in our runs (because accreting systems become much rarer than nonaccreting ones at low redshift, see Figure 12), which makes it difficult to construct a smooth two-dimensional (2D) mass-spin distribution to compare to observations, even by adding together our runs for light and heavy seeds. Figure 15, however, shows that the overall spin evolution of the galaxy population is small at $z < 1$, as a consequence of the reduced galactic activity both in terms of gas cooling/star formation and mergers. Therefore, to improve the statistics of our analysis, we compare observations to $z = 0.1$ to a *fiducial theoretical sample taken at $z = 1$* . For the sake of completeness, effects due to the evolution of the galaxy population at $z < 1$ are investigated in Appendix C, where we show that they do not significantly affect the conclusions of our analysis.

The predicted spin distributions of accreting MBH hosted in spirals at low redshift are shown in Figure 16, together with the measurements of Table 2. The *pseudobulge* model qualitatively reproduces the observed trends, with most of the measurements and relative error bars falling in the 95% confidence region

¹⁶ The Gaussian kernel smoothing has mostly the effect of making the distribution visually smoother, and we checked that the results of our analysis are independent of it.

Table 2
Sample of MBHs with Spin Measurements from the $K\alpha$ Reflection Line

Object Name	Galaxy Type	z	$L_X(\text{erg s}^{-1})$	f_{Edd}	$\log(M_{\text{bh}}(M_{\odot}))$	Spin	Adopted PDF
1H0707–495	...	0.0411	3.7×10^{43}	1.0	6.70 ± 0.4	>0.97	Flat [0.97,0.998]
Mrk1018	S0	0.043	9.0×10^{43}	0.01	8.15	$0.58^{+0.36}_{-0.74}$	Flat [0,0.94]
NGC 4051	SAB(rs)bc	0.0023	3.0×10^{42}	0.03	6.28	>0.99	Flat [0.99,0.998]
NGC 3783	SB(r)ab	0.0097	1.8×10^{44}	0.06	7.47 ± 0.08	>0.88	Flat [0.88,0.998]
1H0419–577	...	0.104	1.8×10^{44}	0.04	8.18 ± 0.05	>0.89	Flat [0.85,0.998]
3C120	S0	0.033	2.0×10^{44}	0.31	$7.74^{+0.20}_{-0.22}$	>0.95	Flat [0.95,0.998]
MCG-6-30-15	E/S0	0.008	1.0×10^{43}	0.4	6.65 ± 0.17	>0.98	hGauss [0.998,0.01]
Ark564	SB	0.0247	1.4×10^{44}	0.11	<6.90	$0.96^{+0.01}_{-0.06}$	hGauss [0.96,0.04]
TonS180	...	0.062	3.0×10^{44}	2.15	$7.30^{+0.60}_{-0.40}$	$0.91^{+0.02}_{-0.09}$	hGauss [0.94,0.067]
RBS1124	...	0.208	1.0×10^{45}	0.15	8.26	>0.97	hGauss [0.998,0.02]
Mrk110	...	0.0355	1.8×10^{44}	0.16	7.40 ± 0.09	>0.89	Gauss [0.945,0.033]
Mrk841	E	0.0365	8.0×10^{43}	0.44	7.90	>0.52	Gauss [0.80,0.17]
Fairall9	Sc	0.047	3.0×10^{44}	0.05	8.41 ± 0.11	$0.52^{+0.19}_{-0.15}$	Gauss [0.6,0.1]
SWIFTJ2127.4+5654	SB0/a(s)	0.0147	1.2×10^{43}	0.18	7.18 ± 0.07	0.6 ± 0.2	Gauss [0.6,0.1]
Mrk79	SBb	0.0022	4.7×10^{43}	0.05	7.72 ± 0.14	0.7 ± 0.1	Gauss [0.7,0.1]
Mrk335	S0a	0.026	5.0×10^{43}	0.25	7.15 ± 0.13	$0.83^{+0.09}_{-0.13}$	Gauss [0.81,0.067,<0.92]
Ark120	Sb/pec	0.0327	3.0×10^{45}	1.27	8.18 ± 0.12	$0.64^{+0.19}_{-0.11}$	Gauss [0.68,0.093]
Mrk359	pec	0.0174	6.0×10^{42}	0.25	6.04	$0.66^{+0.30}_{-0.54}$	Gauss [0.66,0.33,<0.96]
IRAS13224–3809	...	0.0667	7.0×10^{43}	0.71	7.00	>0.987	Gauss [0.989,0.002]
NGC 1365	SB(s)b	0.0054	2.7×10^{42}	0.06	$6.60^{+1.40}_{-0.30}$	$0.97^{+0.01}_{-0.04}$	Gauss [0.97,0.03,<0.98]

Notes. The table is compiled using objects from Reynolds (2014) and Brenneman (2013); galaxy redshifts are taken from the NED database (<http://ned.ipac.caltech.edu/>). Quoted errors in the mass and spin measurements correspond to the 68% and 90% confidence levels, respectively. The spin PDF we use in our statistical analysis is given in the last column, which identifies three different functional forms: flat (min and max value given in []), half-Gaussian (maximum and σ given in []), and Gaussian (maximum and σ given in []). In the latter case, a third number in [], when present, defines a sharp cutoff in the PDF.

predicted by the models. The *disk* model displays a slightly poorer match, with many events outside the 68% confidence region predicted by the model and just a minor hint of the general spindown observed with increasing MBH mass. The *hybrid* model nicely matches the data, reproducing both the observed high-spin subsample and the objects with moderate spin.

6.3. The 2D Kolmogorov–Smirnov Test

Although the qualitative comparison between theoretical models and measurements is encouraging (in the sense that we find the right trends in the right subset of galaxies to reproduce observations) and seems to favor the *hybrid* model over the others, we want to corroborate our findings with some more quantitative indicators. We first performed two-dimensional, one-sample Kolmogorov–Smirnov tests (2D KS; Press et al. 1992) to compare the observed samples to the different MBH subsamples at different redshifts. Although not as rigorous as its one-dimensional counterpart, the test returns an approximate probability, p_{KS} , that the data are drawn from the model distribution (see, Press et al. 1992, for details about the 2D KS statistics).

To account for observational errors, we computed the average p_{KS} over 10^4 realizations of the observed samples, picking the mass and spin of each individual object from the corresponding PDF. Looking at the results shown in Table 3, a number of conclusions can be drawn.

1. The selected subsample matters. In particular, ellipticals and spirals hosting nonaccreting MBHs (i.e., those with $f_{\text{Edd}} < 0.01$) have a spin distribution that poorly matches

Table 3
The 2D KS Test Results on Different Samples of Galaxies for Our Three Fiducial Spin Evolution Models

Model	Ellipticals	Spirals, $f_{\text{Edd}} < 0.01$	Spirals, $f_{\text{Edd}} > 0.01$
<i>Pseudobulge</i>	0.0020	0.0271	0.3614
<i>Disk</i>	0.0015	0.0969	0.0521
<i>Hybrid</i>	0.0016	0.0589	0.5328

Notes. Reported is the (approximate) probability with which the spin measurements can be reproduced by a given model and a given sample. The results for the sample that matches the observations (spirals hosting MBHs with $f_{\text{Edd}} > 0.01$) are highlighted in bold. The theoretical sample is taken at $z = 1$, as explained in the main text.

observations, yielding $p_{\text{KS}} \approx 10^{-3}$ and $p_{\text{KS}} \approx 10^{-2}$ for the *pseudobulge* and *hybrid* models, respectively.

2. In the *hybrid* model, the subsample of accreting MBHs (i.e., ones with $f_{\text{Edd}} > 0.01$) in spirals is perfectly consistent with the observed sample.
3. The *hybrid* model is favored, yielding $p_{\text{KS}} > 0.5$ (we show in Appendix C that this result is independent of binning, redshift, and observational error PDF).
4. The *pseudobulge* model is also consistent with the data, yielding $p_{\text{KS}} > 0.2$.
5. In the *disk* model, the subsample of accreting MBHs in spirals provides a poor match with observations, disfavoring the model.

Some of the above results, in particular those given by the *disk* model, are somewhat bin-dependent. We show in Appendix C that this issue prevents us from ruling out the *disk* model on the

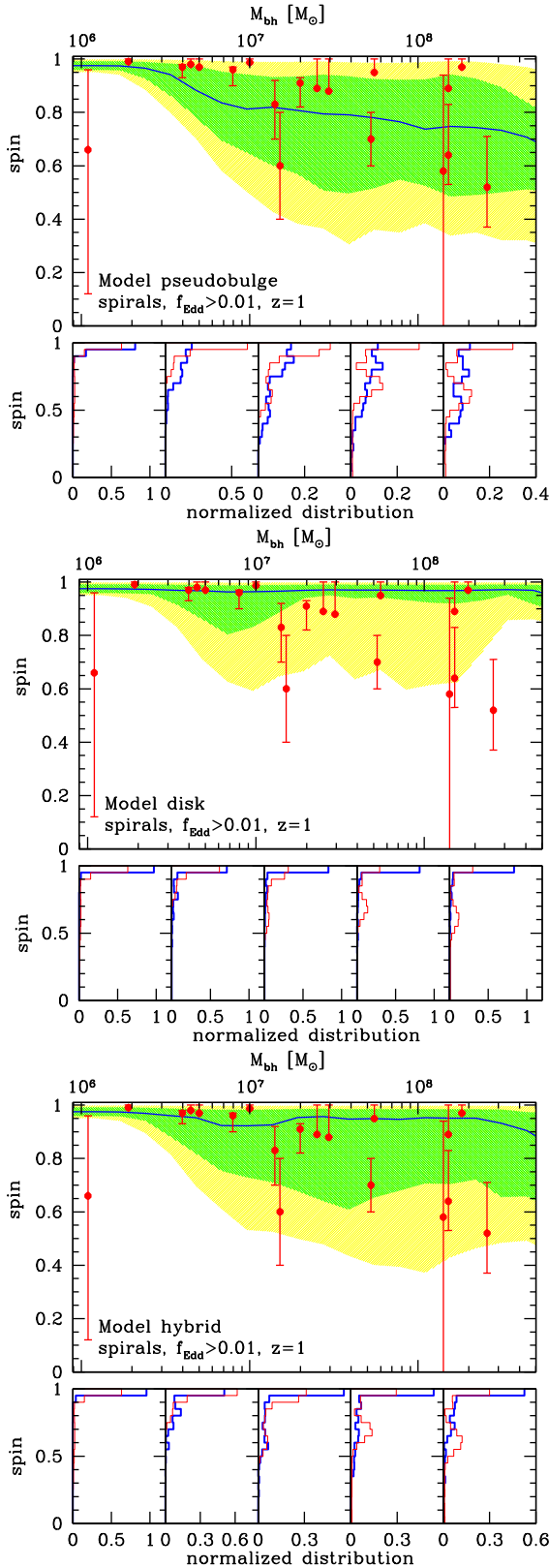


Figure 16. Comparison between measured MBH spins and predictions of our models for the subsample of accreting MBHs ($f_{\text{Edd}} > 0.01$) in spirals. In all three plots, the top panel shows the outcome of the model with the same line and color code as in Figure 15, and red dots are measurements with errors as described in Table 2. The five small bottom panels show the spin distributions predicted by our models in different mass bins (thick blue histograms) and the PDF of the measured spins in the same mass bin, including observation errors (thin red histograms). Theoretical distributions are taken at $z = 1$.

(A color version of this figure is available in the online journal.)

basis of the relatively sparse observed sample, but it does not affect our general conclusions.

6.4. Bayesian Model Selection

The 2D KS test provides useful indications about the consistency of the data with the predictions of a given model. It is, however, not very practical in assessing which one is the best model among a set of different options. This latter issue can be tackled within the framework of Bayesian model selection by computing the posterior probability of the parameters of a certain model, given a set of data. Because our models are non-parametric, this boils down to the evaluation of the odds ratio for different pairs of models, which we now describe.

Following Sesana et al. (2011), we assume that the observations are uncorrelated, so that the number of objects, n_i , measured in a particular $\Delta M_{\text{bh}} \Delta a_{\text{bh}}$ bin in parameter space can be drawn from a Poisson probability distribution with parameter r_i equal to the bin-integrated rate:

$$p(n_i) = \frac{(r_i)^{n_i} e^{-r_i}}{n_i!}. \quad (20)$$

If we divide the parameter space up into a certain number K of bins, then the information that comes from the *data* (D) is the number of events in each bin (n_i). The overall *likelihood* $p(D|X)$ of seeing this data under the model X is the product over all K bins of the Poisson probabilities to see n_i events in the i th bin, given the rate $r_i(X)$ predicted by model X :

$$p(D|X) = \prod_{i=1}^K \frac{(r_i(X))^{n_i} e^{-r_i(X)}}{n_i!}. \quad (21)$$

It is straightforward to take the limit of this expression as the bin sizes tend to zero to derive a continuum version of this equation (Gair et al. 2010), but in this analysis we will stick to binned distributions for simplicity. In the presence of measurement errors, the j th event can then be assigned to different bins, with a probability given by its PDF $\rho_j(M_{\text{bh}}, a_{\text{bh}})$. We can therefore construct the entire set of possible arrays of events falling in each bin, n_i , with their relative probabilities. Each array is then analyzed and weighted according to its probability to get the overall likelihood of the sample, given the model.

If we want to compare two competitive models, A and B , Bayes' theorem allows us to assign to model A a probability

$$p(A|D) = \frac{p(D|A)P(A)}{p(D|A)P(A) + p(D|B)P(B)}, \quad (22)$$

whereas the probability of model B is just obtained by swapping A and B in Equation (22). Here, $p(D|X)$ is the likelihood given by Equation (21), and $P(X)$ is the prior probability assigned to model X . The odds ratio of model A over model B is

$$\Lambda_{AB} = \frac{p(D|A)P(A)}{p(D|B)P(B)}. \quad (23)$$

If we do not have any reason to prefer a priori model A to model B , then $P(A) = P(B) = 0.5$, and the odds ratio becomes the likelihood ratio. Moreover, Equation (22) implies that in a two-model comparison we can simply assign a “relative probability” $p_A = p(D|A)/(p(D|A)+p(D|B))$ to model A and $p_B = 1 - p_A$ to model B .

Table 4

Model Selection Results: Pair Comparisons between Our Three Fiducial Spin Evolution Models, *Pseudobulge* (p), *Disk* (d), and *Hybrid* (h)

Model Pairs	Odds Ratios & Probabilities		
<i>Hybrid/pseudobulge</i>	$\log\Lambda_{hp} = 1.0804$	$p_h = 0.9233$	$p_p = 0.0767$
<i>Hybrid/disk</i>	$\log\Lambda_{hd} = 2.4749$	$p_h = 0.9966$	$p_d = 0.0034$
<i>Pseudobulge/disk</i>	$\log\Lambda_{pd} = 1.3944$	$p_p = 0.9612$	$p_d = 0.0388$

Notes. For each two-model comparison we report the log of the likelihood ratio Λ_{AB} , i.e., the ratio between the probability of model A (p_A) and model B (p_B).

We compute the odds ratios of our three fiducial models: *pseudobulge* (p), *disk* (d), and *hybrid* (h) according to Equation (23), where we assume $P(A) = P(B) = 0.5$. Likelihoods are computed according to Equation (21), folding in measurement errors. The shapes of the error PDFs of each single observation are described in Section 6.1, and we factorize $\rho_j(M_{\text{bh}}, a_{\text{bh}}) = g(M_{\text{bh}})h(a_{\text{bh}})$, assuming uncorrelated mass and spin measurements.

Results are shown in Table 4. We get $\log\Lambda_{hd} \approx 2.5$, implying that the *hybrid* model provides a better description of the data than the *disk* model, at the $>99.5\%$ confidence level. This strengthens the results of the 2D KS test, providing compelling evidence in favor of the *hybrid* model. The *pseudobulge* model sits somewhat in the middle; it is preferred at the $\approx 95\%$ level over the *disk* model, but it is disfavored at about the same level with respect to the *hybrid* model. To summarize, the odds ratio analysis provides moderate (decisive) evidence that the *hybrid* model is a better description of the data than the *pseudobulge* (*disk*) model.

7. DISCUSSION AND CONCLUSIONS

In this paper, we presented the results of a semianalytical model for the evolution of galaxies and MBHs. The model keeps track (although in simplified ways) of the morphology of the galaxies, as well as the MBH masses and spins. For the first time we link the dynamical properties of the gas fueling the MBHs to the host galaxy properties through different observationally based prescriptions and derive predictions testable with existing observations. We stress that all the other similar investigations predicting MBH spin distributions either assumed “chaotic” accretion (MBHs accreting small gas clouds with isotropically oriented angular momenta) or “coherent” accretion (MBHs accreting all the time on a fixed plane).

Our model predicts different spin distributions for different types of galaxies. To date, only ≈ 20 MBH spins have been directly measured through $K\alpha$ iron line fitting (Reynolds 2014; Brenneman 2013). All these MBHs (but one) are hosted in low-redshift late-type galaxies, preventing us from testing our results for different galaxy types. We therefore tested our model by selecting low-redshift accreting MBHs hosted in spirals. For this galaxy class, we have assumed three different gas dynamics prescriptions. In the *pseudobulge* model we assumed that the dynamics of gas fueling the central MBHs is similar to that of the stars in both galaxy bulges or pseudobulges, according to the nature of the host’s spheroidal component. In the *disk* model, instead, the fueling gas has the more coherent dynamics of the large-scale gaseous disk. The *hybrid* model shares the same gas dynamics as the *disk* model for isolated galaxies but assumes a gas dynamics similar to that of stars in spheroids during merger-driven accretion events (see Section 3 for details).

Our models predict interesting features in the MBH spin distribution, and a statistical comparison to observations yields a number of interesting results.

1. Different galaxy morphologies result in different MBH spin distributions. Because the geometrical properties of the accretion flow are related to the large-scale kinematics of the galaxy, MBHs hosted in ellipticals tend to have lower spins than those hosted in spirals.
2. In general, MBH spins are a decreasing function of the MBH mass: $\sim 10^6 M_\odot$ MBHs tend to be maximally spinning, whereas for masses $> 10^8 M_\odot$ a wide range of values is possible for the spin, depending on the host morphology and MBH accretion rate.
3. Accreting MBHs in spirals, i.e., those matching the observational sample, tend to spin fast and do *not* provide an unbiased indicator of the underlying spin distribution of the overall MBH population.
4. The 2D KS tests show that, in general, the *hybrid* and *pseudobulge* models are consistent with observations, while the *disk* model is disfavored. A quantitative assessment of the compatibility of the *disk* model with the data, however, strongly depends on the maximum value to which MBHs can be spun up by accretion. This issue is discussed in detail in Appendix C, where we show that if this value is $a_{\text{bh}} = 0.998$ (Thorne 1974), the *disk* model can be safely ruled out at the $>99\%$ confidence level.
5. A likelihood odds ratio study shows that the *hybrid* model—which takes into account the possible angular momentum reshuffling due to merger-driven phases of nuclear activity—provides the best match to the observed data. In a two-model comparison, (1) it is strongly favored (at the $>99\%$ confidence level) over the *disk* model; and (2) it is moderately favored (only at about the 90% confidence level) over the *pseudobulge* model.
6. For the sake of comparison, in Appendix B we have also run three separate sets of simulations adopting the standard coherent-accretion model, as well as two flavors of the chaotic-accretion model. These models provide a much worse description of the data; the *coherent* model shows features similar to the *disk* model, but with a poorer agreement to the data, while the chaotic models are unambiguously ruled out by observations.

We emphasize that the study of the evolution of the MBH spin distribution in a cosmological framework is still in its infancy. Because our model is idealized from many points of view, here we highlight some still-needed theoretical and observational improvements. (1) The treatment of the Bardeen–Petterson effect, which plays a major role in determining the fraction of prograde versus retrograde accretion events, is based on simple isotropic- α -viscosity-driven accretion disks, and this assumption has been criticized by Sorathia et al. (2013a, 2013b). The impact of this strong and debated assumption is unknown, since no working models of the MBH spin evolution relaxing it are available to date. (2) We assumed that every gas cloud fueling the MBHs weighs $M_{\text{cloud}} \sim 3 \times 10^4 M_\odot$. GMCs are observed to have a broad mass spectrum. Observational studies of local galaxies reported typical molecular cloud mass functions with cutoffs at about 10^5 – $10^6 M_\odot$ (e.g., Williams & McKee 1997; Engargiola et al. 2003; Fukui et al. 2008), making the average cloud mass comparable to the mass that we assume in this paper. We note, however, that the cutoff mass seems to depend on the host galaxy properties (e.g., Hopkins 2012 and references therein).

A simple implementation of a “characteristic” cloud mass function is not trivial and beyond the scope of this paper. The effect of different average cloud masses can anyway be easily understood: the cloud mass contributes to setting the maximum MBH mass at which a complete alignment of the spin occurs at every accretion event, effectively making the fueling dynamics unimportant. To first approximation (see D13 for a more detailed discussion), an order-of-magnitude variation of the average cloud mass results in an order-of-magnitude shift along the MBH mass axis of all the spin distributions. The results not showing any significant feature in the spin evolution (e.g., the $f_{\text{Edd}} > 0.01$ *disk* model at low redshift, but see also the *coherent* and *chaotic I* models discussed in Appendix B) would thus remain mostly unchanged under a variation of the cloud mass. On the other hand, the *pseudobulge* and *hybrid* models would predict higher spins for higher masses (lower spins for lower masses) if the cloud mass were higher (lower). We checked that a shift of the spin distributions by one order of magnitude toward larger masses does not affect the compatibility of those two models with the data, yielding a KS probability $p_{\text{KS}} > 0.3$. A similar shift of the distribution toward lower masses results in a slightly worse description of the data, but still with a KS probability $\gtrsim 0.1$. (3) Our dynamical prescriptions for the nuclear gas dynamics are mostly based on gas and/or stellar dynamics observations on scales much larger than the accretion disk or the MBH sphere of influence. Our model would greatly benefit from a description of the gas dynamics on scales $\lesssim 100$ pc, already achievable in some cases with high-resolution ALMA spectroscopy (e.g., Combes et al. 2013, 2014). Finally, (4) in our model we completely neglected the effect of rotational energy extraction from the MBH on the spin. This could in principle power relativistic jets through the Blandford–Znajek mechanism, limiting the maximum spin to lower values in radio galaxies.

From an observational point of view, the main improvement would consist in enlarging the currently small sample of measured MBH spins and extending it to higher redshift and different galaxy types¹⁷. In this regard, the forthcoming Astro-H satellite will have exquisite combined spectral resolution and sensitivity, making $K\alpha$ -based spin measurements possible perhaps up to $z \sim 1$ (Takahashi et al. 2012). Along the same lines, *Athena+*, to be launched in 2028, will push such measurements to $z \sim 2$ for extremely X-ray bright systems, significantly expanding the observed spin sample (Dovciak et al. 2013). On a shorter timescale, the *eROSITA* satellite will observe $> 10^5$ AGNs. Image stacking in luminosity and redshift bins will reveal the “average” shape of the $K\alpha$ line of these systems, making it possible to study trends in the typical spin of AGNs across a large mass range and for redshifts perhaps up to $z \sim 1$ (Merloni et al. 2012), thus providing an important benchmark for comparison to theoretical models. On a different note, the *eLISA* mission, now selected by ESA for the L3 launch slot, will measure the spins of merging MBH binaries across the cosmic history to high precision, providing a sample that will not be biased toward high X-ray luminosities.

Even though the future of spin measurements looks literally bright, we should also keep in mind that the uncertainties on the value of measured spins depend on the technique used. Different methods have been used to constrain the MBH spin distribution at different redshifts and for different masses. Some methods estimate the spin value from the radio properties of the AGNs (e.g., Daly & Sprinkle 2014 and references therein), from the ionizing flux required to produce the observed broad emission lines (Netzer & Trakhtenbrot 2014), or from fitting the continuum from the accretion disk (Laor & Davis 2011b). Some of these methods are still a matter of debate (e.g., Gallo et al. 2012; Raimundo et al. 2012; Laor & Davis 2011a), and all of them require an independent measure of the MBH mass to estimate its spin. In this paper we compared our predictions with the mass-independent measurements obtained through relativistically broadened iron $K\alpha$ line fitting to prevent any possible spurious mass-spin correlation. We refer to Reynolds (2014) and Brenneman (2013) for a detailed discussion of the uncertainties of these measurements. Since our models predict a significant dependence of the MBH spins on the MBH masses, the uncertainties on the masses are fundamental as well. For example, Mrk 359 has an estimated mass of $\approx 10^6 M_{\odot}$, obtained through a single-epoch measurement of the continuum and broad $H\beta$ FWHM (Zhou & Wang 2005). The width of the line is only 480 km s^{-1} , significantly smaller than both the typical value for type 1 AGNs and the threshold for being classified as a NLS1. Since the MBH is hosted in a spiral galaxy, the line is peculiarly large to be associated with a single narrow line, and a broad component is expected because of the point-like emission clearly visible in the *Hubble Space Telescope* imaging (Malkan et al. 1998). The observed line width could be so narrow because of orientation effects, already suggested to be significant for NLS1s (Decarli et al. 2008), causing an underestimation of the MBH mass. (To be on the safe side, we checked that the contribution of Mrk 359 to our analysis is negligible. Its MBH spin is so poorly constrained that removing it from the observational sample has no effect on our results.) More independent measurements of the masses of MBHs with spin estimates would help better constrain their values. The detection of gravitational waves will also greatly improve the situation, giving high-precision measurements of both the MBH masses and spins, which could be compared with predictions for merging systems.

Regardless of the large uncertainties on which we commented above, it is remarkable that two of the models (*pseudobulge* and *hybrid*) that we investigated generate samples of MBH masses and spins consistent with observations. Since these models assume that the accreting gas has less coherent dynamics than the larger-scale gas structure (although, in the hybrid case, only in recent merger remnants), our analysis seems to suggest the existence of a physical process that, while decreasing the gas-angular momentum magnitude (triggering accretion in the first place), reshuffles the gas-angular momentum direction as well. Such a reshuffling could be caused by local processes, i.e., star formation and the torques exerted by the gas self-gravity (e.g., Maio et al. 2013), as well as larger-scale gravitational instabilities and violent gas inflows (e.g., Hopkins et al. 2012; Dubois et al. 2014b). On the other hand, in order to achieve such a good agreement between the predictions of the model and the observed spins, we have to require the accreting gas to have, on average, a nonzero angular momentum, i.e., the gas must *not* accrete isotropically onto the MBH. We have in fact shown that a perfectly isotropic accretion flow would result in

¹⁷ While finalizing this manuscript, Reis et al. (2014) reported a spin measurement of the $z = 0.658$ lensed quasar 1RXS J113151.6–12315 of $a = 0.87^{+0.08}_{-0.15}$ (3σ errors). The estimated MBH mass is $2 \times 10^8 M_{\odot}$, the accretion rate computed from its bolometric luminosity is nearly Eddington, and the host is a Seyfert 1 spiral galaxy (Claeskens et al. 2006). Thus, this system falls in our sample of accreting spirals at $z = 1$ shown in Figure 16, and its inferred mass and spins are perfectly consistent with all the models shown there.

significantly lower spins for intermediate to large MBH masses, which is inconsistent with observations (see Appendix B).

We further note that the *pseudobulge* and the *hybrid* models, while providing the best descriptions of the data, hint at different (although possibly coexisting) evolutionary scenarios. The hybrid scenario has the highest statistical significance and a simple physical interpretation, with a clear candidate for the source of turbulence. The gas dynamics remains quite coherent for most of the time, which is reasonable because gas can efficiently dissipate turbulent motions on few local orbital times (see the discussion in Maio et al. 2013 and references therein). Only during galaxy mergers the violent reshuffling of the angular momentum allows for more isotropic gas inflows. We note that, strictly speaking, in the *hybrid* model we adopt a “bulge-like” dynamics for the accreting gas during the *whole* of the merger-driven accretion events, even though the AGN activity lasts for longer than the galaxy merger itself. Thus, during the tails of the nuclear activity, accretion may be more coherent than in our model’s assumptions. However, during a merger-driven AGN phase, most of the gas is accreted in a short, almost-Eddington burst, lasting about a Salpeter time $\lesssim 0.2$ Gyr. The long-lived accretion tails, still observable at low redshifts, present instead a lower Eddington ratio $f_{\text{Edd}} \sim 0.01$ and cannot therefore significantly change the MBH spin magnitude.

Although the pseudobulge model is disfavored by our statistical analysis, it still provides a good description of the observational data and is consistent with the evidence that low-redshift AGNs with moderate-to-high Eddington ratios are preferentially hosted in pseudobulges (Heckman & Best 2014). Pseudobulges have recently been associated with stellar bars, i.e., structures able to drive gas inflows toward the galaxy nucleus (see, e.g., Sellwood 2014; Kormendy 2013, for up to date reviews). After the initial instability responsible for the bar formation, the bar itself generally undergoes a thickening that can be either caused by a second “buckling” instability or by a vertical resonance (Sellwood 2014), possibly responsible for the pseudobulge formation (Kormendy 2013). In this scenario, the gas could accrete with a more disk-like dynamics until the bar thickens and fall toward the MBH with a higher-velocity dispersion after the pseudobulge forms if the buckling instability and/or any vertical resonances significantly affect the gas motion.

The paucity of data and the many uncertainties about the different fueling processes do not allow us to firmly reject either of these models. If either model is confirmed by more data, it could point toward a physically motivated galaxy–MBH coevolution scenario for low-redshift disk galaxies, in which the dynamics of gas in nuclear bars and/or mergers drive the MBH mass and spin evolution.

We are indebted to M. R. Krumholz and D. Calzetti for invaluable insights into the metallicity dependency of star formation. We also thank M. Colpi, J. Gair, M. Kesden, A. Merloni, C. Reynolds, A. Tchekhovskoy, and M. Volonteri for insightful comments and discussions. E.B. acknowledges support from the European Union’s Seventh Framework Program (FP7/PEOPLE-2011-CIG) through the Marie Curie Career Integration Grant GALFORMBHS PCIG11-GA-2012-321608 and support from the Deutsches Zentrum für Luft- und Raumfahrt (DLR) through the DFG Grant SFB/TR 7 Gravitational Wave Astronomy. Computations were performed on the GPC supercomputer at the SciNet HPC Consortium, as well as on the “Projet Horizon Cluster” at the Institut d’astrophysique de Paris.

APPENDIX A STAR FORMATION

Observations of our and nearby galaxies have established that star formation is ultimately associated with GMCs, *giant* because they can be very massive ($M \sim 10^6 M_\odot$) and extended (~ 100 pc). There the star formation rate is determined by the mass fraction f_c in cold gas (generally, but not only, in molecular form) and the timescale t_{SF} needed to convert it into stars. This latter depends both on the cloud properties, such as density (the higher the density, the faster is the process) and on the presence of feedback-driven turbulence, which slows the collapse. One of the main (observationally supported) assumptions is that the GMC properties are environment-independent, as long as the surrounding ISM has lower pressure than the GMC itself. In particular, the cloud surface density Σ_{cl} is set by internal processes to be always around $\Sigma_{\text{cl}} \approx 85 M_\odot \text{ pc}^{-2}$ in more tenuous environments, where the gas surface density is $\Sigma_g \leq 85 M_\odot \text{ yr}^{-1} \equiv \Sigma_{\text{th}}$ (e.g., Bolatto et al. 2011). Above this threshold, pressure equilibrium between the ISM and the GMC sets $\Sigma_{\text{cl}} \simeq \Sigma_g$.

A.1. Star Formation in the Galactic Disk

In this framework, the local star formation in the galactic disk can be described by

$$\dot{\Sigma}_* = \frac{f_c \Sigma_g}{t_{\text{SF}}}, \quad (\text{A1})$$

where the timescale t_{SF} has two regimes, according to whether the cloud density Σ_{cl} is set by the interstellar pressure,

$$t_{\text{SF}}^{-1} = \frac{M_6^{-0.33}}{0.8 \text{ Gyr}} \max \left[1, \left(\frac{\Sigma_g}{\Sigma_{\text{th}}} \right)^{0.67} \right], \quad (\text{A2})$$

(Krumholz et al. 2009), where $M_6 = M/(10^6 M_\odot)$ is the GMC mass. The local Jeans mass $M_j \approx \sigma_g^2/G^2\Sigma_g$ gives a good estimate of the cloud mass, where σ_g is the gas velocity dispersion. In a galactic *disk* environment, we may assume a condition of marginal gravitational stability and obtain a function of the background gas surface density only,

$$t_{\text{SF}}^{-1} = (2.6 \text{ Gyr})^{-1} \times \begin{cases} \left(\frac{\Sigma_g}{\Sigma_{\text{th}}} \right)^{-0.33}, & \Sigma_g < \Sigma_{\text{th}}, \\ \left(\frac{\Sigma_g}{\Sigma_{\text{th}}} \right)^{0.34}, & \Sigma_g > \Sigma_{\text{th}}. \end{cases} \quad (\text{A3})$$

The cold-gas mass fraction f_c is equivalent to the molecular mass fraction at metallicity greater than $\sim 1\%$ solar, when H_2 has time to form before collapsing and forming stars. At lower metallicities, instead, star formation will occur in a cold-atomic-gas phase rather than a molecular phase (Krumholz 2012). In general, as the metallicity decreases, the cold gas available for forming stars decreases as well. However, recent observations of nearby spirals and dwarfs (Bigiel et al. 2010) and of the Small Magellanic Cloud (Bolatto et al. 2011) suggest that f_c levels off at around 2% rather than dropping to zero. These considerations led us to adopt the following prescription,

$$f_c = \begin{cases} 1 - \left[1 + \left(\frac{3}{4} \frac{s}{1+s} \right)^{-5} \right]^{-1/5}, & \text{if } f_c > 2\%, \\ 2\%, & \text{otherwise} \end{cases} \quad (\text{A4})$$

(M. R. Krumholz, 2013 private communication), with

$$s = \ln(1 + 0.6\chi)/(0.04\Sigma_1 Z'),$$

$$\chi = 0.77(1 + 3.1Z^{0.365}),$$

$$\delta = 0.0712(0.1s^{-1} + 0.675)^{-2.8},$$

where $\Sigma_1 = \Sigma_g/(M_\odot \text{ pc}^{-2})$ and Z' is the metallicity in Solar units.

Integrating Equation (A1) over the entire disk surface, we obtain the total star formation rate in the disk.

A.2. Star Formation in the Galactic Bulges

The very same prescription can be applied to the bulge during the periods of “quiescent star formation” in the galaxy, i.e., when violent star-bursting events are not triggered. Practically, we use a volumetric star formation law,

$$\dot{\rho}_* = \frac{f_c \rho_g}{t_{\text{SF}}}, \quad (\text{A5})$$

which we derive directly from Equation (A1), by expressing Σ_g and M as a function of the volumetric gas density ρ_g and the local isothermal sound speed c_s .

Let us start by considering the star formation timescale (Equation (A2)). In regions with densities below threshold, $t_{\text{SF}} \propto M_j^{0.33}$, where we can simply write the Jeans mass in the more familiar way,

$$M_j = \frac{\pi}{6} \frac{c_s^3}{G^{3/2} \rho_g^{1/2}} \approx 10^6 M_\odot \left(\frac{c_s}{8.3 \text{ km s}^{-1}} \right)^3 \rho_1^{-1/2}, \quad (\text{A6})$$

with $\rho_1 = \rho_g/(M_\odot \text{ pc}^{-3})$. In denser regions of the bulge, one has an additional dependence on Σ_{cl} , i.e., $t_{\text{SF}} \propto M_j^{0.33} \Sigma_{\text{cl}}^{-0.67}$ (see Equation (A2)). To relate the surface density to the volume density, let us note that for a spherical cloud of mass M and characteristic size L , $\rho_{\text{cl}} \approx M/L^3$ and $L \approx \Sigma_{\text{cl}}/\rho_{\text{cl}}$. Eliminating L in these two expressions, we obtain $\rho_{\text{cl}} \approx M_\odot \text{ pc}^{-3} (\Sigma_{\text{cl}}/\Sigma_{\text{th}})^{3/2} M_6^{-1/2}$. Inserting Equation (A6) and recalling the pressure equilibrium condition, $\rho_g \approx \rho_{\text{cl}}$ (Krumholz & McKee 2005), we finally get

$$\left(\frac{\Sigma_g}{\Sigma_{\text{th}}} \right) = \rho_1^{1/2} \left(\frac{c_s}{8.3 \text{ km s}^{-1}} \right). \quad (\text{A7})$$

Thus, the overall timescale expression becomes

$$t_{\text{SF}}^{-1} = (0.8 \text{ Gyr})^{-1} \times \begin{cases} \rho_1^{0.165} \left(\frac{c_s}{8.3 \text{ km s}^{-1}} \right)^{-0.99} & \Sigma_g < \Sigma_{\text{th}}, \\ \rho_1^{1/2} \left(\frac{c_s}{8.3 \text{ km s}^{-1}} \right)^{-0.32} & \Sigma_g > \Sigma_{\text{th}}. \end{cases} \quad (\text{A8})$$

We now turn our attention to the fraction f_c of mass in cold gas available for star formation (Equation (A4)). Unlike t_{SF} , f_c depends on the *gas* density and *not* on the GMC density. In more tenuous regions, out of pressure equilibrium, the cloud can be denser than the background gas, i.e., $\eta \equiv \rho_{\text{cl}}/\rho_g \geq 1$. Therefore, in principle, in Equation (A4) we should use a modified version of Equation (A7), e.g., an expression $\Sigma_g \propto \eta^{-1/3} \rho_g^{1/2} c_s$, which could be used both above ($\eta \approx 1$) and *below* threshold. However, since f_c has a floor of 2% (see Equation (A4)), which kicks in when η takes values of a few to several, the modification factor ($\eta^{-1/3} \approx 1-2$) is negligible relative to the other uncertainties in the derivation of Equation (A7). We will therefore always directly use Equation (A7) in Equation (A4), whether above or below threshold.

A.2.1. Starburst in Merging Galaxies

Observations suggest a link between starbursts and mergers. The main evidence is that the strongest starbursts (ultraluminous and hyperluminous infrared galaxies) are predominantly merging systems at all redshifts (e.g., Elbaz & Cesarsky 2003). More recently, CO observations of galaxy populations hinted that starburst/merging galaxies have a different, more efficient star formation law (Daddi et al. 2010; Genzel et al. 2010). We therefore assume that in merging systems the star formation is driven by different dynamical processes in the bulge which induce star formation over a dynamical time. In practice, we use the same procedure as in B12: in the gaseous bulge that forms after the merger, star formation is regulated by

$$\dot{\rho}_* = \frac{\rho_g}{t_{\text{ff}}}, \quad (\text{A9})$$

where $t_{\text{ff}} = \sqrt{3\pi/(32G\rho_g)}$ is the local dynamical time for the gas. Again, this expression can be integrated over the bulge volume to yield the total star formation rate.

APPENDIX B

COHERENT AND CHAOTIC ACCRETION SCENARIOS

Alongside our fiducial models, for the sake of comparison we also investigate three models implementing the coherent and chaotic scenarios often used in the literature.

1. *Coherent model*. Each accretion event takes place in a well-defined plane, persisting for the duration of the episode and efficiently spinning-up the hole (Thorne 1974); see for instance, the coherent model of Berti & Volonteri (2008).
2. *Chaotic I model*. For each accretion event, we always take $F = w = 0.5$, independently of the accreted mass (see for instance, the chaotic model of Berti & Volonteri 2008)¹⁸.
3. *Chaotic II model*. The model of this paper, but with $F = 1/2$, i.e., with isotropic distribution for the angular momentum of the gas clouds (King & Pringle 2006).

The overall redshift evolution of the MBH spin distributions for the *coherent*, *chaotic I*, and *chaotic II* models is shown in Figure 17 (to be compared to Figure 15). In the *coherent* model, MBHs tend to be maximally spinning irrespective of redshift, accretion rate, and galaxy host morphology. The opposite is true for the *chaotic I* model, where spins tend to be small ($a_{\text{bh}} < 0.5$) and cluster around zero. In the *chaotic II* model, there is a transition between maximally spinning MBHs at low masses and nonspinning MBHs at high masses. The difference from the *chaotic I* model is that each accreting lump of matter has a defined angular momentum (although with random direction); light MBHs thus align with it and are efficiently spun up, whereas massive MBHs do not and effectively experience zero-angular momentum accretion averaged over many episodes.

The features in the spin distribution discussed above already hint at the difficulty of reconciling these three models with observations. We do not show here a visual comparison, but we report the results of the same statistical analysis performed in Sections 6.3 and 6.4. In this case we summed up accreting MBH in spirals *and* in ellipticals when building spin distributions. The procedure does not affect the results because in these simplistic

¹⁸ Note that, in our framework, once F is given, w cannot be arbitrarily set to 0.5, because it is a function of the MBH and cloud-angular momenta through Equation (13). In this respect, the *chaotic I* model corresponds to the limiting case where $F = 0.5$ and $M_{\text{disk}} \rightarrow 0$ (which implies $J_{\text{disk}} \rightarrow 0$).

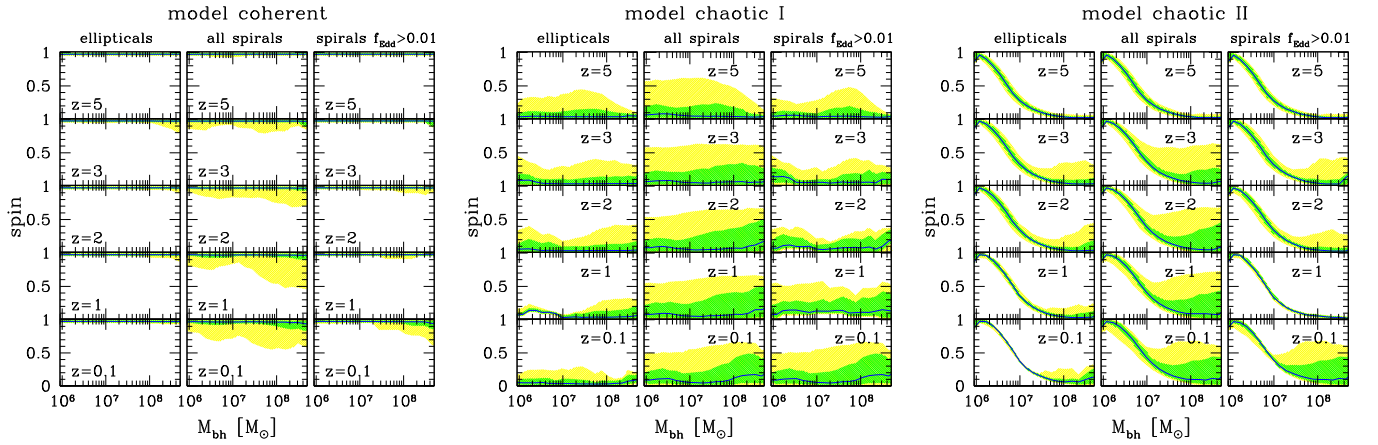


Figure 17. Same as Figure 15 but for the *coherent*, *chaotic I*, and *chaotic II* models, as specified at the top of each panel. In each plot, the blue line is the median of the spin distribution as a function of the MBH mass and as predicted by the model, while green and yellow shaded areas represent the spin ranges enclosing 68% and 95% of the distribution.

(A color version of this figure is available in the online journal.)

Table 5
The 2D KS Test Results on Different Samples of Galaxies for All Spin Evolution Models under Different Assumptions about the Theoretical Distribution's Computation and the Treatment of Observational Errors (Indicated in the First Column)

Assumptions	Pseudobulge			Disk			Hybrid			Coherent	Chaotic I	Chaotic II
	E	S	S acc	E	S	S acc	E	S	S acc	S + E acc	S + E acc	S + E acc
$z = 1/10a_{\text{bh}}/\text{Flat}$	0.0034	0.0280	0.2336	0.0034	0.0969	0.1969	0.0035	0.0577	0.5831	0.0685	$<10^{-4}$	$<10^{-4}$
$z = 1/10a_{\text{bh}}/\text{Gauss}$	0.0015	0.0247	0.2468	0.0015	0.0793	0.1945	0.0015	0.0488	0.6094	0.0719	$<10^{-4}$	$<10^{-4}$
$z = 1/20a_{\text{bh}}/\text{Gauss}$	0.0020	0.0271	0.3614	0.0015	0.0969	0.0521	0.0016	0.0589	0.5328	0.0035	$<10^{-4}$	$<10^{-4}$
$z = 1/30a_{\text{bh}}/\text{Gauss}$	0.0015	0.0302	0.3785	0.0015	0.0986	0.0232	0.0016	0.0598	0.3761	0.0007	$<10^{-4}$	$<10^{-4}$
$z = 0.5/10a_{\text{bh}}/\text{Gauss}$	0.0019	0.0197	0.2666	0.0018	0.0615	0.1186	0.0020	0.0379	0.5636	0.0869	$<10^{-4}$	$<10^{-4}$
$z = 0.5/20a_{\text{bh}}/\text{Gauss}$	0.0020	0.0223	0.3816	0.0018	0.0743	0.0170	0.0019	0.0451	0.4380	0.0063	$<10^{-4}$	$<10^{-4}$
$z = 0.5/30a_{\text{bh}}/\text{Gauss}$	0.0018	0.0258	0.4251	0.0018	0.0735	0.0069	0.0019	0.0447	0.2764	0.0013	$<10^{-4}$	$<10^{-4}$
$z = 0.1/10a_{\text{bh}}/\text{Gauss}$	0.0021	0.0164	0.0813	0.0023	0.0454	0.0711	0.0024	0.0278	0.6620	0.0656	$<10^{-4}$	$<10^{-4}$
$z = 0.1/20a_{\text{bh}}/\text{Gauss}$	0.0021	0.0181	0.0984	0.0023	0.0526	0.0035	0.0024	0.0322	0.6699	0.0028	$<10^{-4}$	$<10^{-4}$
$z = 0.1/30a_{\text{bh}}/\text{Gauss}$	0.0018	0.0217	0.0899	0.0023	0.0534	0.0007	0.0023	0.0324	0.4392	0.0005	$<10^{-4}$	$<10^{-4}$

Notes. For the *pseudobulge*, *disk*, and *hybrid* models, we compared existing spin measurements with theoretical distributions (produced with our model) for ellipticals (E), spirals (S), an spirals containing accreting MBHs (S acc); these latter are highlighted in bold as they match the properties of the observational sample), whereas for the *coherent*, *chaotic I*, and *chaotic II* models, we sum all accreting MBHs (S+E acc) to achieve better statistics.

models the spin evolution is not connected to the nature of the host galaxy, and it allows us to increase the size of the theoretical sample. The *coherent* model shows properties similar to the *disk* one, but with a stronger clustering toward maximally spinning MBHs, resulting in a poorer match to the data, quantified by a KS probability $p_{\text{KS}} < 10^{-2}$. Both the *chaotic I* and *chaotic II* models result in very different distributions favoring low spins (as shown in the bottom right panels of Figure 17), which are impossible to reconcile with observations ($p_{\text{KS}} < 10^{-4}$ in both cases; see numbers in Table 5). This is confirmed by the computation of the odds ratios against, e.g., the *hybrid* model, which completely discard all three scenarios.

APPENDIX C

SANITY CHECKS ON THE STATISTICAL ANALYSIS

As explained in the main text, to carry out our analysis we used our model to construct discrete theoretical distributions on a specific grid in the $M_{\text{bh}}-a_{\text{bh}}$ parameter space. We then compared spin measurements at $z < 0.1$ to theoretical predictions at $z = 1$. In this appendix, we show that our conclusions do not depend significantly on these specific choices.

As mentioned, we choose to compare observations to theoretical distributions at $z = 1$ rather than at $z = 0.1$ in order to have a larger statistical sample. The idea behind this choice is that theoretical distributions should not change significantly at $z < 1$, where QSO and AGN activity and star formation are fading. This is shown to indeed be the case in the left panel of Figure 18, where we plot the redshift evolution of the population of accreting MBHs in spirals for different mass bins and models. The figure shows that distributions generated with the *pseudobulge* and *hybrid* models do not change much at $z \leq 1$, but the effect of the small statistical sample at low redshifts is clear, especially at $z = 0.1$ (thin blue histograms) for the *pseudobulge* model. Distributions generated with the *disk* model are slightly more redshift-dependent. At $z = 0.1-0.5$ (thin blue and medium green histograms) they show more clustering at almost maximal spins, and the moderate spin tails present at $z = 1$ (thick red histograms) are suppressed. (As we will show below, this has an impact when estimating the model's compatibility with the data).

For the analysis of the main text, we evaluated theoretical distribution on a grid made of five equally log-spaced mass bins and 20 linear bins covering the spin range $0 < a_{\text{bh}} < 1$. We construct here distributions using instead 10 and 30 linear a_{bh}

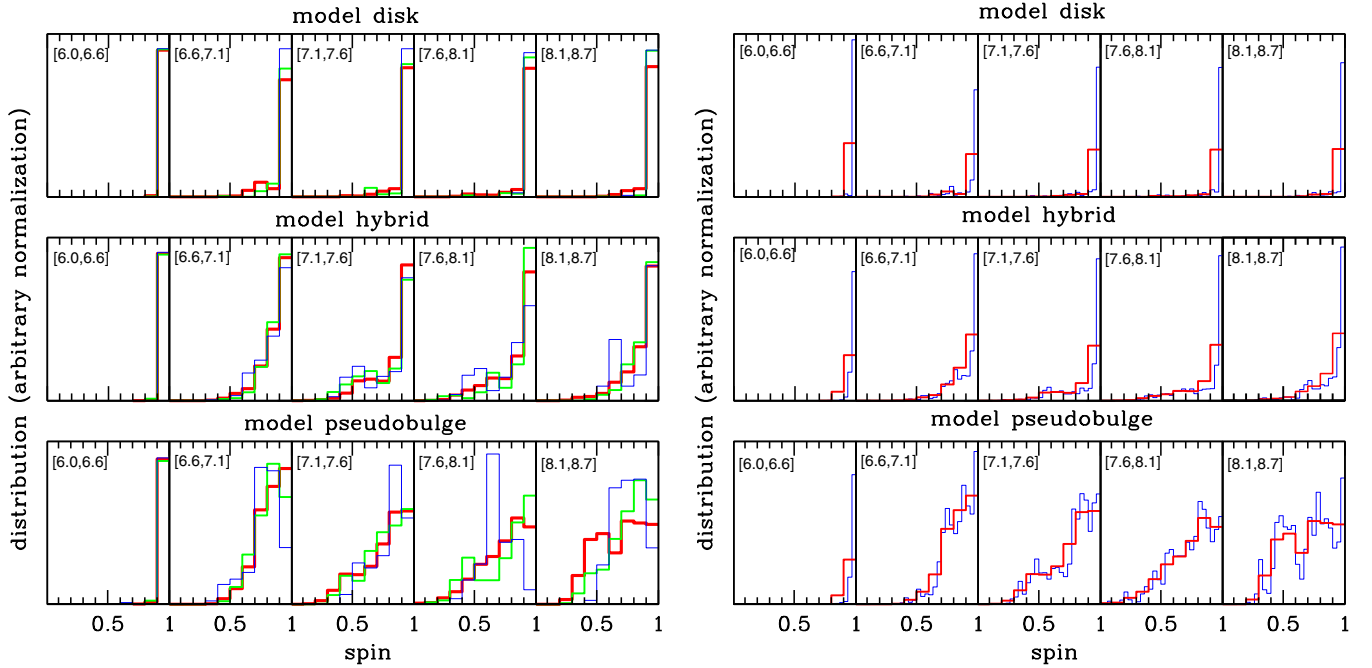


Figure 18. Left panels show spin distributions in different mass bins for accreting MBHs in spirals for our three fiducial models. In each panel, histograms are for $z = 1$ (thick–red), $z = 0.5$ (medium–green), and $z = 0.1$ (thin–blue). The numbers in square parentheses in each panel represent the extremes of the considered $\log M_{\text{bh}}$ interval. The right panels show spin distributions in different MBH mass bins and at $z = 1$, but now considering different a_{bh} binnings. Thick red and thin blue histograms are computed using 10 and 30 a_{bh} bins, respectively. The numbers in square parentheses in each panel represent the extremes of the considered $\log M_{\text{bh}}$ interval.

(A color version of this figure is available in the online journal.)

bins (by keeping 5 mass bins) and also considering 20 bins both in mass and spin. In the right panel of Figure 18, we show the dependence of the distributions on the a_{bh} binning. The distributions for the *disk* and *hybrid* models both depend on the binning at the high-spin end. This is not surprising because the two models adopt similar accretion prescriptions for MBHs in spirals that recently experienced galactic-disk instabilities. However, as we show below, in the *hybrid* model this binning dependence does not have a large impact on the comparison with the data. This is because a significant tail at moderate spins is guaranteed by the fact that the model is also partly *pseudobulge* in nature (see the model description in Section 3.2).

Being aware of these issues, we assess here the impact of the theoretical sample’s binning and redshift on the results of our statistical analysis. Results for the 2D KS tests are reported in Table 5. The *hybrid* and *pseudobulge* models yield probabilities that are largely independent on the choice of binning and redshift. We just notice a significant discrepancy at $z = 0.1$ in the subsample of accreting MBHs in spirals in the *pseudobulge* case. This is entirely due to the small number of objects found in our simulations that cause a very noisy distribution. The *chaotic I* and *chaotic II* models are also unaffected by the specific redshift and binning choice and are always ruled out at high significance. Conversely, the match between the *disk* and *coherent* models and observations is binning-dependent. Although apparently problematic, this dependence has a physical origin. In our thin accretion disk model, the maximum MBH spin is $a_{\text{bh}} = 0.998$ (Thorne 1974). Basically, all the simulated MBHs falling in the highest a_{bh} bin indeed have this spin value. By binning the spin distribution, we are “spreading” those systems on the width of the bin; the larger the bin, the larger the spread, making it easier to reconcile the theoretical distribution with the large number of spins measured in the $[0.85, 1]$ range (see Table 2). If the

maximum MBH spin is indeed $a_{\text{bh}} = 0.998$, then the finest spin binning should provide the most trustworthy results. We caution, however, that such a narrow spin distribution, peaked close to the maximal spin $a_{\text{bh}} = 1$, is affected by some simplifications that we made in our spin evolution model. As described in Sections 2.2 and 3.3, we assumed (1) that at the beginning of each accretion episode the MBH spin is parallel to the total angular momentum of the reservoir and (2) that whenever $J_{\text{disk}}/2J_{\text{bh}} > 1$, the alignment process is very fast, and accretion is effectively coherent. Relaxing these two assumptions would affect the highly spinning MBHs, because when $a_{\text{bh}} \approx 1$, a small amount of retrograde accretion can efficiently spin the black hole down. The effect of relaxing assumption (1) has already been discussed in Section 3.3, so here we will simply estimate the effect of relaxing prescription (2). For a broad range of MBH masses, $J_{\text{disk}}/2J_{\text{bh}}$ can be larger than, but still close to, 1. In these cases, if the accretion event is initially misaligned with respect to \mathbf{J}_{bh} by more than $\pi/2$, accretion would be retrograde during the first part of the spin realignment process. If a fraction of 10% of the gas mass were accreted on retrograde orbits, the equilibrium spin would be the same as in the case $F \approx 0.9$ when neglecting the spin realignment, i.e., $a_{\text{eq}} \approx 0.9$ (see Figure 3). Such an effect has been observed and discussed in studies where the spin direction was evolved during each single-accretion event (Dotti et al. 2010; D13). Furthermore, different accretion disk models allow MBH spins only up to $a_{\text{bh}} = 0.9\text{--}0.95$ (e.g., Gammie et al. 2004), and efficient angular momentum extraction via jets might set a maximum equilibrium spin lower than $a_{\text{bh}} = 0.9$ (see, e.g., Moderski & Sikora 1996; Moderski et al. 1998). It is therefore impossible to completely rule out the *disk* and *coherent* models.

We also checked the outcome of the Bayesian model comparison for the different assumptions; results are shown in Table 6. As expected from the 2D KS tests, the consistency of the *disk*

Table 6
Model Selection Results: Comparisons between the *Pseudobulge* (p), *Disk* (d), and *Hybrid* (h) Models

Assumptions	Hybrid/Pseudobulge			Hybrid/Disk			Pseudobulge/Disk		
	$\log\Lambda_{hp}$	P_{hybrid}	$P_{pseudobulge}$	$\log\Lambda_{hd}$	P_{hybrid}	P_{disk}	$\log\Lambda_{pd}$	$P_{pseudobulge}$	P_{disk}
$z = 1/10a_{bh}/Flat$	0.7995	0.8631	0.1369	1.9259	0.9883	0.0117	1.1264	0.9304	0.0696
$z = 1/10a_{bh}/Gauss$	1.1391	0.9323	0.0677	2.0634	0.9914	0.0086	0.9242	0.8936	0.1064
$z = 1/20a_{bh}/Gauss$	1.0804	0.9233	0.0767	2.4749	0.9966	0.0034	1.3944	0.9612	0.0388
$z = 1/30a_{bh}/Gauss$	0.9119	0.8909	0.1091	2.8313	0.9985	0.0015	1.9193	0.9881	0.0119
$z = 0.5/10a_{bh}/Gauss$	1.0901	0.9248	0.0715	3.0761	0.9992	0.0008	1.9860	0.9898	0.0102
$z = 0.5/20a_{bh}/Gauss$	0.9016	0.8886	0.1114	4.1259	0.9999	0.0001	3.2243	0.9994	0.0006
$z = 0.5/30a_{bh}/Gauss$	0.0543	0.5312	0.4687	2.9997	0.9990	0.0010	2.9454	0.9988	0.0012
$z = 0.1/10a_{bh}/Gauss$	2.3982	0.9960	0.0040	11.241	>0.9999	$<10^{-11}$	8.8435	>0.9999	$<10^{-8}$
$z = 0.1/20a_{bh}/Gauss$	2.5955	0.9975	0.0025	22.541	1.0	0.0	19.945	1.0	0.0
$z = 0.1/30a_{bh}/Gauss$	3.7300	0.9998	0.0002	22.597	1.0	0.0	18.867	1.0	0.0

Notes. For each two-model comparison, we report the log of the likelihood ratio Λ_{AB} , i.e., the ratio between the probability of model A (p_A) and model B (p_B).

model with observations is highly dependent on the binning size of the distribution. This is confirmed by our model selection exercise, which shows that both $\log\Lambda_{pd}$ and $\log\Lambda_{hd}$ generally increase with the number of a_{bh} bins. Note that *for any choice of binning and sample redshift*, $\log\Lambda_{hd} > 2$, implying that the *hybrid* model always provides a better description of the data than the *disk* model, at least at the 99% confidence level. This is particularly interesting, because even though the *disk* model computed on 10 a_{bh} bins at $z = 1$ passes the 2D KS test with flying colors (see Table 5), the odds ratio test provides compelling evidence in favor of the *hybrid* model. The *pseudobulge* model sits somewhat in the middle; it is generally preferred at the 90%–99% level over the *disk* model, but is disfavored at about the same level with respect to the *hybrid* model (with the anomaly of the $z = 0.5$, 30 a_{bh} bins). To summarize, the odds ratio analysis always provides moderate (decisive) evidence that the *hybrid* model is a better description of the data than the *pseudobulge* (*disk*) model, thus proving that our main results are independent of the particular choice of binning and redshift of the theoretical samples.

REFERENCES

- Barausse, E. 2012, *MNRAS*, **423**, 2533, (erratum 440, 1295 [2014])
 Barausse, E., Morozova, V., & Rezzolla, L. 2012, *ApJ*, **758**, 63 (erratum 786, 76 [2014])
 Barausse, E., & Rezzolla, L. 2009, *ApJL*, **704**, L40
 Barausse, E., & Sotiriou, T. P. 2013, *CQGra*, **30**, 244010
 Bardeen, J. M., & Petterson, J. A. 1975, *ApJL*, **195**, L65
 Begelman, M. C., Blandford, R. D., & Rees, M. J. 1980, *Natur*, **287**, 307
 Bernardi, M., Meert, A., Sheth, R. K., et al. 2013, *MNRAS*, **436**, 697
 Bernardi, M., Shankar, F., Hyde, J. B., et al. 2010, *MNRAS*, **404**, 2087
 Berti, E., & Volonteri, M. 2008, *ApJ*, **684**, 822
 Bigiel, F., Leroy, A., Walter, F., et al. 2010, *AJ*, **140**, 1194
 Blandford, R. D., & McKee, C. F. 1982, *ApJ*, **255**, 419
 Blandford, R. D., & Znajek, R. L. 1977, *MNRAS*, **179**, 433
 Bolatto, A. D., Leroy, A. K., Jameson, K., et al. 2011, *ApJ*, **741**, 12
 Bonoli, S., Mayer, L., & Callegari, S. 2014, *MNRAS*, **437**, 1576
 Bower, R. G., Benson, A. J., Malbon, R., et al. 2006, *MNRAS*, **370**, 645
 Brenneman, L. 2013, in *Measuring the Angular Momentum of Supermassive Black Holes* (New York: Springer)
 Brenneman, L. W., Reynolds, C. S., Nowak, M. A., et al. 2011, *ApJ*, **736**, 103
 Broderick, A. E., Loeb, A., & Narayan, R. 2009, *ApJ*, **701**, 1357
 Broderick, A. E., & Narayan, R. 2006, *ApJL*, **638**, L21
 Buonanno, A., Kidder, L. E., & Lehner, L. 2008, *PhRvD*, **77**, 026004
 Calderone, G., Ghisellini, G., Colpi, M., & Dotti, M. 2013, *MNRAS*, **431**, 210
 Cappellari, M., Emsellem, E., Bacon, R., et al. 2007, *MNRAS*, **379**, 418
 Castignani, G., Haardt, F., Lapi, A., et al. 2013, *A&A*, **560**, A28
 Claeskens, J.-F., Sluse, D., Riaud, P., & Surdej, J. 2006, *A&A*, **451**, 865
 Cole, S., Helly, J., Frenk, C. S., & Parkinson, H. 2008, *MNRAS*, **383**, 546
 Combes, F., García-Burillo, S., Casasola, V., et al. 2013, *A&A*, **558**, A124
 Combes, F., García-Burillo, S., Casasola, V., et al. 2014, *A&A*, **565**, A97
 Conselice, C. J. 2006, *MNRAS*, **373**, 1389
 Croton, D. J., Springel, V., White, S. D. M., et al. 2006, *MNRAS*, **365**, 11
 Daddi, E., Elbaz, D., Walter, F., et al. 2010, *ApJL*, **714**, L118
 Daly, R. A., & Sprinkle, T. B. 2014, *MNRAS*, **438**, 3233
 Decarli, R., Dotti, M., Fontana, M., & Haardt, F. 2008, *MNRAS*, **386**, L15
 De Lucia, G., & Blaizot, J. 2007, *MNRAS*, **375**, 2
 Dotti, M., Colpi, M., Pallini, S., Perego, A., & Volonteri, M. 2013, *ApJ*, **762**, 68
 Dotti, M., Volonteri, M., Perego, A., et al. 2010, *MNRAS*, **402**, 682
 Dovciak, M., Matt, G., Bianchi, S., et al. 2013, arXiv:1306.2331
 Dubois, Y., Volonteri, M., & Silk, J. 2014a, *MNRAS*, **440**, 1590
 Dubois, Y., Volonteri, M., Silk, J., Devriendt, J., & Slyz, A. 2014b, *MNRAS*, **440**, 2333
 Elbaz, D., & Cesarsky, C. J. 2003, *Sci*, **300**, 270
 Engargiola, G., Plambeck, R. L., Rosolowsky, E., & Blitz, L. 2003, *ApJS*, **149**, 343
 Epinat, B., Tasca, L., Amram, P., et al. 2012, *A&A*, **539**, A92
 Fabricius, M. H., Saglia, R. P., Fisher, D. B., et al. 2012, *ApJ*, **754**, 67
 Fanidakis, N., Baugh, C. M., Benson, A. J., et al. 2011, *MNRAS*, **410**, 53
 Fanidakis, N., Baugh, C. M., Benson, A. J., et al. 2012, *MNRAS*, **419**, 2797
 Ferrarese, L., & Merritt, D. 2000, *ApJL*, **539**, L9
 Forbes, J. C., Krumholz, M. R., Burkert, A., & Dekel, A. 2014, *MNRAS*, **443**, 168
 Förster Schreiber, N. M., Genzel, R., Bouché, N., et al. 2009, *ApJ*, **706**, 1364
 Fukui, Y., Kawamura, A., Minamidani, T., et al. 2008, *ApJS*, **178**, 56
 Gair, J. R., Tang, C., & Volonteri, M. 2010, *PhRvD*, **81**, 104014
 Gallo, E., Russell, D., & Fender, R. 2012, in *Proc. Half a Century of X-ray Astronomy, 2012 September 12–21, Mykonos Island, Greece* (available online at <http://www.astro.noa.gr/xcosmo/>)
 Gammie, C. F., Shapiro, S. L., & McKinney, J. C. 2004, *ApJ*, **602**, 312
 Gebhardt, K., Bender, R., Bower, G., et al. 2000, *ApJL*, **539**, L13
 Genzel, R., Tacconi, L. J., Gracia-Carpio, J., et al. 2010, *MNRAS*, **407**, 2091
 Ghez, A. M., Salim, S., Weinberg, N. N., et al. 2008, *ApJ*, **689**, 1044
 Gibbons, G. 1975, *CMAh*, **44**, 245
 Gillessen, S., Eisenhauer, F., Trippe, S., et al. 2009, *ApJ*, **692**, 1075
 Gnerucci, A., Marconi, A., Cresci, G., et al. 2011, *A&A*, **528**, A88
 Goldreich, P., & Julian, W. H. 1969, *ApJ*, **157**, 869
 Granato, G. L., De Zotti, G., Silva, L., Bressan, A., & Danese, L. 2004, *ApJ*, **600**, 580
 Gültekin, K., Richstone, D. O., Gebhardt, K., et al. 2009, *ApJ*, **698**, 198
 Guo, Q., White, S., Boylan-Kolchin, M., et al. 2011, *MNRAS*, **413**, 101
 Haiman, Z., Ciotti, L., & Ostriker, J. P. 2004, *ApJ*, **606**, 763
 Hänni, R. S. 1982, *PhRvD*, **25**, 2509
 Häring, N., & Rix, H.-W. 2004, *ApJL*, **604**, L89
 Heckman, T., & Best, P. 2014, *ARA&A*, **52**, 589
 Heckman, T. M., Kauffmann, G., Brinchmann, J., et al. 2004, *ApJ*, **613**, 109
 Hickox, R. C., Jones, C., Forman, W. R., et al. 2009, *ApJ*, **696**, 891
 Hicks, E. K. S., & Malkan, M. A. 2008, *ApJS*, **174**, 31
 Hopkins, P. F. 2012, *MNRAS*, **423**, 2016
 Hopkins, P. F., Hernquist, L., Hayward, C. C., & Narayanan, D. 2012, *MNRAS*, **425**, 1121
 Hopkins, P. F., Richards, G. T., & Hernquist, L. 2007, *ApJ*, **654**, 731
 Kaspi, S., Maoz, D., Netzer, H., et al. 2005, *ApJ*, **629**, 61
 Kassim, S. A., Weiner, B. J., Faber, S. M., et al. 2012, *ApJ*, **758**, 106

- Kauffmann, G., & Heckman, T. M. 2009, *MNRAS*, **397**, 135
- Kerr, R. P. 1963, *PhRvL*, **11**, 237
- Khandai, N., Di Matteo, T., Croft, R., et al. 2014, arXiv:1402.0888
- King, A. R., Lubow, S. H., Ogilvie, G. I., & Pringle, J. E. 2005, *MNRAS*, **363**, 49
- King, A. R., & Pringle, J. E. 2006, *MNRAS*, **373**, L90
- Kormendy, J. 2013, in *Secular Evolution of Galaxies*, ed. J. Falcón-Barroso & J. H. Knapen (Cambridge: Cambridge Univ. Press), 1
- Kormendy, J., & Richstone, D. 1995, *ARA&A*, **33**, 581
- Krumholz, M. R. 2012, *ApJ*, **759**, 9
- Krumholz, M. R., & Gnedin, N. Y. 2011, *ApJ*, **729**, 36
- Krumholz, M. R., & McKee, C. F. 2005, *ApJ*, **630**, 250
- Krumholz, M. R., McKee, C. F., & Tumlinson, J. 2009, *ApJ*, **699**, 850
- Kuhlen, M., Madau, P., & Krumholz, M. R. 2013, *ApJ*, **776**, 34
- Lagos, C. D. P., Padilla, N. D., & Cora, S. A. 2009, *MNRAS*, **395**, 625
- Laor, A., & Davis, S. 2011a, arXiv:1110.0653
- Laor, A., & Davis, S. W. 2011b, *MNRAS*, **417**, 681
- Lapi, A., Raimundo, S., Aversa, R., et al. 2014, *ApJ*, **782**, 69
- Law, D. R., Steidel, C. C., Erb, D. K., et al. 2009, *ApJ*, **697**, 2057
- Li, Y.-R., Wang, J.-M., & Ho, L. C. 2012, *ApJ*, **749**, 187
- Lousto, C. O., & Zlochower, Y. 2009, *PhRvD*, **79**, 064018
- Lusso, E., Comastri, A., Simmons, B. D., et al. 2012, *MNRAS*, **425**, 623
- Magorrian, J., Tremaine, S., Richstone, D., et al. 1998, *AJ*, **115**, 2285
- Maio, U., Dotti, M., Petkova, M., Perego, A., & Volonteri, M. 2013, *ApJ*, **767**, 37
- Malkan, M. A., Gorgjian, V., & Tam, R. 1998, *ApJS*, **117**, 25
- Maoz, E. 1998, *ApJL*, **494**, L181
- Marconi, A., & Hunt, L. K. 2003, *ApJL*, **589**, L21
- Marinucci, A., Matt, G., Kara, E., et al. 2014a, *MNRAS*, **440**, 2347
- Marinucci, A., Matt, G., Miniutti, G., et al. 2014b, *ApJ*, **787**, 83
- McConnell, N. J., & Ma, C.-P. 2013, *ApJ*, **764**, 184
- Merloni, A., Predehl, P., Becker, W., et al. 2012, arXiv:1209.3114
- Merloni, A., Rudnick, G., & Di Matteo, T. 2004, *MNRAS*, **354**, L37
- Miyoshi, M., Moran, J., Herrnstein, J., et al. 1995, *Natur*, **373**, 127
- Moderski, R., & Sikora, M. 1996, *MNRAS*, **283**, 854
- Moderski, R., Sikora, M., & Lasota, J.-P. 1998, *MNRAS*, **301**, 142
- Nandra, K., Barret, D., Barcons, X., et al. 2014, in *General Relativity, Cosmology, and Astrophysics*, Vol. 177, ed. J. Bicák & T. Ledvinka (Cham, Switzerland: Springer), 523
- Narayan, R., McClintock, J. E., & Tchekhovskoy, A. 2013, arXiv:1303.3004
- Netzer, H., & Trakhtenbrot, B. 2014, *MNRAS*, **438**, 672
- Newman, E. T., Couch, E., Chinnappared, K., et al. 1965, *JMP*, **6**, 918
- Newman, S. F., Genzel, R., Förster Schreiber, N. M., et al. 2013, *ApJ*, **767**, 104
- Pani, P., & Cardoso, V. 2009, *PhRvD*, **79**, 084031
- Pani, P., Macedo, C. F., Crispino, L. C., & Cardoso, V. 2011, *PhRvD*, **84**, 087501
- Perego, A., Dotti, M., Colpi, M., & Volonteri, M. 2009, *MNRAS*, **399**, 2249
- Press, W. H., Teukolsky, S. A., Vetterling, W. T., & Flannery, B. P. 1992, *Numerical Recipes in FORTRAN: The Art of Scientific Computing* (Cambridge: Cambridge Univ. Press)
- Raimundo, S. I., Fabian, A. C., Vasudevan, R. V., Gandhi, P., & Wu, J. 2012, *MNRAS*, **419**, 2529
- Reis, R. C., Reynolds, M. T., Miller, J. M., & Walton, D. J. 2014, *Natur*, **507**, 207
- Reynolds, C. S. 2014, *SSRv*, **183**, 277
- Rezzolla, L., Barausse, E., Dorband, E. N., et al. 2008, *PhRvD*, **78**, 044002
- Risaliti, G., Harrison, F. A., Madsen, K. K., et al. 2013, *Natur*, **494**, 449
- Ruderman, M. A., & Sutherland, P. G. 1975, *ApJ*, **196**, 51
- Scannapieco, E., Silk, J., & Bouwens, R. 2005, *ApJL*, **635**, L13
- Schödel, R., Ott, T., Genzel, R., et al. 2002, *Natur*, **419**, 694
- Sellwood, J. A. 2014, *RvMP*, **86**, 1
- Sesana, A., Gair, J., Berti, E., & Volonteri, M. 2011, *PhRvD*, **83**, 044036
- Shankar, F. 2013, *CQGra*, **30**, 244001
- Shankar, F., Salucci, P., Granato, G. L., De Zotti, G., & Danese, L. 2004, *MNRAS*, **354**, 1020
- Shankar, F., Weinberg, D. H., & Miralda-Escudé, J. 2009, *ApJ*, **690**, 20
- Shankar, F., Weinberg, D. H., & Miralda-Escudé, J. 2013, *MNRAS*, **428**, 421
- Sikora, M., Stawarz, L., & Lasota, J.-P. 2007, *ApJ*, **658**, 815
- Soltan, A. 1982, *MNRAS*, **200**, 115
- Sorathia, K. A., Krolik, J. H., & Hawley, J. F. 2013a, *ApJ*, **777**, 21
- Sorathia, K. A., Krolik, J. H., & Hawley, J. F. 2013b, *ApJ*, **768**, 133
- Swinbank, A. M., Sobral, D., Smail, I., et al. 2012, *MNRAS*, **426**, 935
- Takahashi, T., Mitsuda, K., Kelley, R., et al. 2012, *Proc. SPIE*, **8443**, 84431Z
- Tchekhovskoy, A., Narayan, R., & McKinney, J. C. 2010, *ApJ*, **711**, 50
- The eLISA Consortium, Seoane, P. A., Aoudia, S., et al. 2013, arXiv:1305.5720
- Thorne, K. S. 1974, *ApJ*, **191**, 507
- van Meter, J. R., Miller, M. C., Baker, J. G., Boggs, W. D., & Kelly, B. J. 2010, *ApJ*, **719**, 1427
- Volonteri, M., Madau, P., Quataert, E., & Rees, M. J. 2005, *ApJ*, **620**, 69
- Volonteri, M., Sikora, M., & Lasota, J.-P. 2007, *ApJ*, **667**, 704
- Volonteri, M., Sikora, M., Lasota, J.-P., & Merloni, A. 2013, *ApJ*, **775**, 94
- Wang, J.-M., Hu, C., Li, Y.-R., et al. 2009, *ApJL*, **697**, L141
- Wilkins, S. M., Trentham, N., & Hopkins, A. M. 2008, *MNRAS*, **385**, 687
- Williams, J. P., & McKee, C. F. 1997, *ApJ*, **476**, 166
- Wilman, D. J., Fontanot, F., De Lucia, G., Erwin, P., & Monaco, P. 2013, *MNRAS*, **433**, 2986
- Wisnioski, E., Glazebrook, K., Blake, C., et al. 2011, *MNRAS*, **417**, 2601
- Yagi, K., Yunes, N., & Tanaka, T. 2012, *PhRvD*, **86**, 044037
- Zhou, X.-L., & Wang, J.-M. 2005, *ApJL*, **618**, L83